WELLBORE INTEGRITY AND CEMENT SHEATH DEBONDING ANALYSIS FOR WELLS IN THE EUGENE ISLAND OPD, GULF OF MEXICO

By

JARRETT LEE WISE

Bachelor of Arts in Physics

Hastings College

Hastings, NE

2014

Submitted to the Faculty of the
Graduate College of the
Oklahoma State University
in partial fulfillment of
the requirements for
the Degree of
MASTER OF SCIENCE
May 2019

WELLBORE INTEGRITY AND CEMENT SHEATH DEBONDING ANALYSIS FOR WELLS IN THE EUGENE ISLAND OPD, GULF OF MEXICO

Thesis Approved:

Dr. Runar Nygaard

Thesis Adviser

Dr. Geir Hareland

Dr. Prem Bikkina

ACKNOWLEDGEMENTS

I would like to start off by thanking my advisor, Dr. Runar Nygaard, for the guidance and support he has given me through this process. His help, both professional and otherwise, will always be appreciated. I hope to repay the favor with helping him choose his March Madness brackets in the following years.

I would also like to thank Dr. Geir Hareland and Dr. Prem Bikkina for their time and effort as part of my graduate committee and taking the time to review this thesis. I would also like to thank my friends and coworkers especially, ACed, for their time, entertainment, and friendship.

Lastly I would like to thank my family for their love, support, and encouragement through this process. The many years of school and numerous destinations along the way couldn't have been done without their support.

Name: Jarrett Lee Wise

Date of Degree: MAY, 2019

Title of Study: WELLBORE INTEGRITY AND CEMENT SHEATH DEBONDING ANALYSIS FOR WELLS IN THE EUGENE ISLAND OPD, GULF OF MEXICO

Major Field: Petroleum Engineering

Abstract: The Gulf of Mexico (GoM) is home to more than 50,000 oil and gas wells with approximately 30,000 wells that are plugged and abandoned leading to concerns of oil and gas leakage where currently, little to no monitoring is performed. The cement used when completing and eventually plugging wells is subjected to harsh conditions leading to failure of the cement due to debonding of the cement to the formation and/or casing, shrinkage of the cement, and chemical degradation in the cement. The goal of this study is to identify and rank the contributing factors of stress development that influence the potential of debonding along the cement interfaces for wells in the Eugene Island OPD in the GoM using staged poro-elastic Finite Element Models (FEM). The results show that the setting stress and the pore pressure in the cement that develop during hydration cause the most potential for debonding whereas the geographic in-situ stress magnitudes and cement mechanical properties have minimal effect on the stress development.

TABLE OF CONTENTS

Chapter Page

Chapter Page

Chapter Page

LIST OF TABLES

Table Page

LIST OF FIGURES

Figure Page

Figure Page

Figure Page

Figure Page

NOMENCLATURE

Symbol	Description
σ	Stress, Normal Stress, MPa
F	Force, N
A	Area, m^2
F_N	Normal Force, MPa
F_S	Shear Force, N
τ	Shear Stress, N
σ_x	Normal Stress in x, MPa
σ_y	Normal Stress in y, MPa
σ_z	Normal Stress in z, MPa
τ_{xy}	Shear Stress in xy, MPa
τ_{yx}	Shear Stress in yx, MPa
τ_{xz}	Shear Stress in xz, MPa
τ_{zx}	Shear Stress in zx, MPa
τ_{yz}	Shear Stress in yz, MPa
τ_{zy}	Shear Stress in zy, MPa
σ_1	Principal Stress 1, MPa
σ_2	Principal Stress 2, MPa
σ_3	Principal Stress 3, MPa
σ_V	Vertical/overburden Stress, MPa
σ_h	Minimum Horizontal Stress, MPa
σ_H	Maximum Horizontal Stress, MPa
$\rho(z)$	Bulk Density at Depth z
g	Acceleration Due to Gravity
dz	Depth Increment
σ'	Effective Stress, MPa
P_P	Pore Pressure, MPa
α	Biot's Coefficient
ϵ	Strain, unitless
L	Length
ϵ_x	Strain in x
E	Young's Modulus, Pa
υ	Poisson's Ratio, unitless
σ_θ	Hoop Stress, MPa
σ_r	Radial Stress, MPa
σ_z	Vertical Stress, MPa

$\tau_{r\theta}$	Shear Stress in rθ , MPa
$\tau_{\theta z}$	Shear Stress in θz, MPa
τ_{rz}	Shear Stress in rz, MPa
R_w	Wellbore Radius, m
r	Radius of Interest, m
P_w	Pressure, MPa
σ'_θ	Effective Hoop Stress, MPa
σ'_r	Effective Radial Stress, MPa
σ'_z	Effective Vertical Stress, MPa
$\tau'_{r\theta}$	Effective Shear Stress in rθ , MPa
τ_f	Shear Strength, MPa
τ_o	Cohesion, MPa
ϕ	Angle of Internal Friction
μ	Coefficient of Internal Friction
β	Failure Angle
τ'	Effective Shear Stress
P	Pressure, MPa

CHAPTER I

INTRODUCTION

As part of the life cycle in regards to oil and gas operations, wells are taken off production and are abandoned. With the maturity of many oil and gas provinces around the world, field abandonment activities are on the rise. The requirements of wellbore abandonment vary from region to region. The likelihood of leakage in plugged and abandoned (P&A) wells is not well established, and oil companies are not required to monitor for leakage.

Wellbores are designed with steel casing and cement to prevent leakage and to maintain wellbore integrity. The cement is placed in the annulus between the casing and the formation when a well is completed and serves dual purposes: the cement is responsible to hold and support the casing in place and to provide zonal isolation between formation fluids of different zones (Nelson, 1990; Smith, 1984; Smith, 1987). The annulus between the casing and the borehole can be cemented from the bottom of a casing string to the surface but other times, wells are only partially cemented in hydrocarbon or freshwater zones to provide zonal isolation. Therefore, the integrity of the cement is critical in preventing leakage. The cement sheath can become damaged due to events and conditions during cementing operations or in response to physical and/or chemical changes after cementing. Examples are changes in temperature and internal casing pressures, deterioration of the cement during construction, production, or during and after P&A (Ravi et al.,

2002; Nygaard et al., 2011). Even in a wellbore with complete cement fluid displacement and the cement sheath covering the full annulus, leakage pathways may develop due to tensile or shear fractures in the cement sheath, or as microannuli caused from debonding along the casing/cement and/or cement/rock formation interfaces. Leakage pathways can be placed into two categories: primary and secondary (Weideman, 2014). The primary leakage pathways are pathways that are created during the cementing job. The primary pathways include:

1) An incomplete annular cementing job that does not reach the seal layer (Bois et al., 2011).
2) A lack of cement plug or permanent packer (Watson and Bachu, 2009).
3) Failure of the casing by burst or collapse (Cooke et al., 1983).
4) Poor cement bonding caused by mudcake (Bois et al., 2011).
5) Channeling in the cement (Nelson and Guillot, 2006).
6) Primary permeability in the cement sheath or cement plug (Cooke et al., 1983).

The secondary leakage pathways occur later after the cement job is complete. These pathways are:

7) Debonding due to tensile stress on the casing/cement and cement/rock interfaces (Bois et al., 2012)
8) Fractures in the cement and/or rock formation (Bois et al., 2012).
9) Chemical dissolution and carbonation of the cement (Nygaard et al., 2011).
10) Wear or corrosion of the casing (Watson and Bachu, 2009; Nygaard et al., 2011).

The various leakage pathways that can occur in the near wellbore region are shown in Figure 1.1.

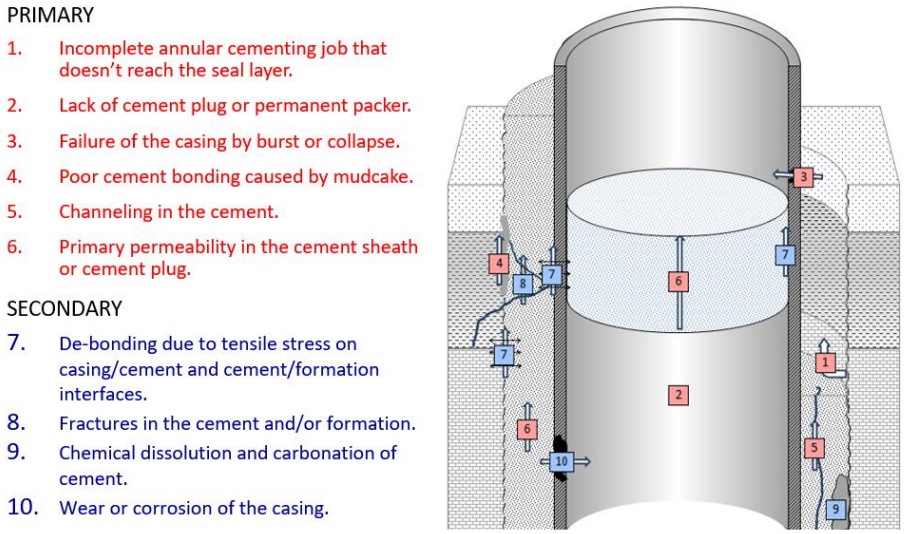

Figure 1.1: Primary and secondary leakage pathways in the near wellbore region (Weideman 2014).

Checking for wellbore leakage in offshore wells in the Gulf of Mexico (GoM) is difficult due to the water depths of hundreds of feet up to 10,000 feet. When these offshore wells are permanently P&A'ed, the well's casing is cut below the sea floor. If any leakage were to occur, it would have to be measured on the sea floor. Otherwise, leakage would be diluted by seawater and spread away from the original location by currents and tides. Dilution of the leakage combined with the sheer number of P&A'ed wells in the GoM (> 30,000) makes it challenging to determine the exact location for a leaking well. Due to such factors, quantitative data on wellbore leakage is not available thus leading to the need for numerical models that can be used to estimate the likelihood of a well leaking as well as the amount of hydrocarbon leakage.

The objective of this thesis is to determine the leakage potential of P&A'ed wells in the GoM to provide input to risk analyses models to determine potential leakage quantities in lieu of actual measured leakage data. The deliverable of this project is to identify and rank the contributing factors of stress development by importance that influence wellbore leakage through the cement sheath through the mechanism of debonding. Knowing the contributing factors that affect stress development that ultimately lead to cement sheath failure can lead to designing enhanced cements that are less likely to fail.

In the following chapters, a review of the background and literature will be presented in Chapter 2. Chapter 3 will describe the Gulf of Mexico and the study location for the case studies. The Finite Element Model (FEM) methodology and parameters used within the model will be discussed in Chapter 4. The analytical and FEM results will be presented and discussed in Chapter 5. Conclusions will be given in Chapter 6.

CHAPTER II

LITERATURE STUDY

2.1. OVERVIEW OF PRIMARY CEMENTING OPERATIONS

Primary cementing is the process of placing cement within the annulus between the casing and formations exposed to the wellbore (Nelson, 1990). This cement is known as the cement sheath and has a dual purpose; the cement sheath supports the casing and provides zonal isolation between formation fluids of different zones (Nelson, 1990; Smith, 1984; Smith, 1987). The cement acts as a hydraulic seal in the annular space between the cement and formation. This seal needs to be in full contact between the two interfaces in order to prevent channels from forming thus preventing leakage through the cement sheath. The formation of channels requires additional cementing operations which are likely to be costly, time-consuming, and may damage the wellbore.

The basic process for performing a primary cement job uses a two-plug method after drilling a well section to the desired depth (Smith, 1987). During drilling, drilling fluid is used to remove cuttings and to provide wellbore stability. After the desired depth is reached, the drill pipe is removed, and casing is inserted into the hole while the drilling fluid remains in the hole. The objective of the primary cement job is to displace drilling fluid and replace it with cement. When the cement is in a pumpable fluid-like state, it is called a cement slurry. The process of replacing the drilling fluid with the cement slurry usually uses the two-plug cementing method. Two plugs are used to isolate the cement slurry as it is pumped through the casing and prevent it from coming

in contact with the drilling fluid. One plug is placed between the cement slurry and drilling fluid while the other follows the cement slurry and prevents any displacement fluids from coming in contact with the slurry. If the cement slurry and drilling fluid/displacement fluids come into contact, the cement slurry would become contaminated and the mechanical and/or chemical properties may change, potentially leading to undesired effects. The plugs also serve another purpose; they act as wipers to help remove any drilling fluid from the rock formation allowing the cement to come into direct contact with the rock. Enough cement slurry is pumped such that the annular column is filled from the bottom of the casing to past any production/freshwater zones. The cement slurry may be pumped such that it fills the annular space from the bottom of the casing string to the surface depending on the stability and depth of the wellbore. Once the slurry is pumped to the desired locations, the well is left shut in to allow the cement to hydrate and harden.

2.2. ROCK AND CEMENT MECHANICS

The well placed in the subsurface is constructed with steel casing and cement sheaths in the annular space between the casing and the surrounding rock formation. This chapter reviews the subsurface stresses, mechanical properties, and failure mechanisms for the materials used within and surrounding the well.

2.2.1. STRESSES IN THE SUBSURFACE

The theory behind the rock mechanics used in this chapter stem from work presented in Fjaer et al. (2008) and Jaeger et al. (2007). For this thesis, hardened cement is considered similar to the mechanical nature of rocks, and both are assumed to behave elastically. Both hardened cement and rocks behave linear elastically in that they are able to recover from deformation produced by forces so long as the changes in forces are small. For the theory behind elasticity, it

will be assumed that rocks and hardened cement are analogous terms. In subsequent chapters, a clear distinction between the two will be made.

The theory of elasticity in regards to rock mechanics consists of two major concepts: stress and strain. Stress is defined in Equation 2.1 and states that the stress of a material (σ) is equal to the force (F) acting through the cross-sectional area divided by the cross-sectional area (A).

$$\sigma = \frac{F}{A} \tag{2.1}$$

The SI units of stress are Pascal (Pa). The sign convention for stress used in the petroleum industry and this thesis are that compressive stresses are positive while tensile stresses are negative. Two examples of stress are shown in Figure 2.1 in which a stress is applied perpendicular to a cylindrical sample, and an example in which stress is applied at an angle.

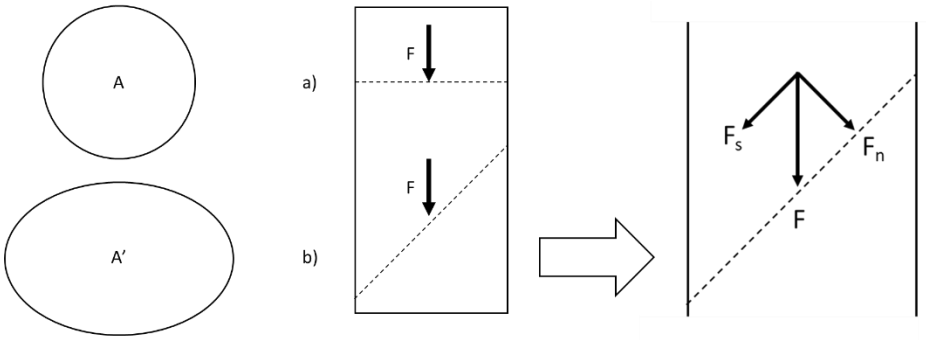

Figure 2.1: Two perspectives of stress on a cylindrical sample. A) the cross-sectional area for the two stresses. B) the force applied normal to the sample (a) and at an angle (b). C) the force components for the stress applied at an angle (b).

Stress is considered a tensor in which it is described as a magnitude and direction with reference to the plane (cross-sectional area) it acts across. The magnitude is composed of directional dependent components. If a force is no longer normal to the cross-section, such as in Figure 2.1 (C), then the force needs to be broken down into components: normal and shear force. The normal force is perpendicular to the cross-section while the shear force is parallel to the cross-

section. The resulting force components are used in Equation 2.1 to determine normal (σ) and shear (τ) stresses. The normal and shear stresses are shown in Equations 2.2 and 2.3 respectively.

$$\sigma = \frac{F_n}{A} \tag{2.2}$$

$$\tau = \frac{F_s}{A} \tag{2.3}$$

Using a Cartesian coordinate system, the stress components for a 3D cube will be composed of normal and shear stresses along each axis. The normal stress components are perpendicular to the axis while the shear stress components are parallel to the axis. The 3D stress tensor is composed of nine stress components which are shown in Figure 2.2. The 3D stress tensor consists of three normal (σ_x, σ_y, σ_z) and six shear (τ_{xy}, τ_{yx}, τ_{xz}, τ_{zx}, τ_{yz}, τ_{zy}) stress components. The 3D stress tensor matrix is shown in Equation 2.4.

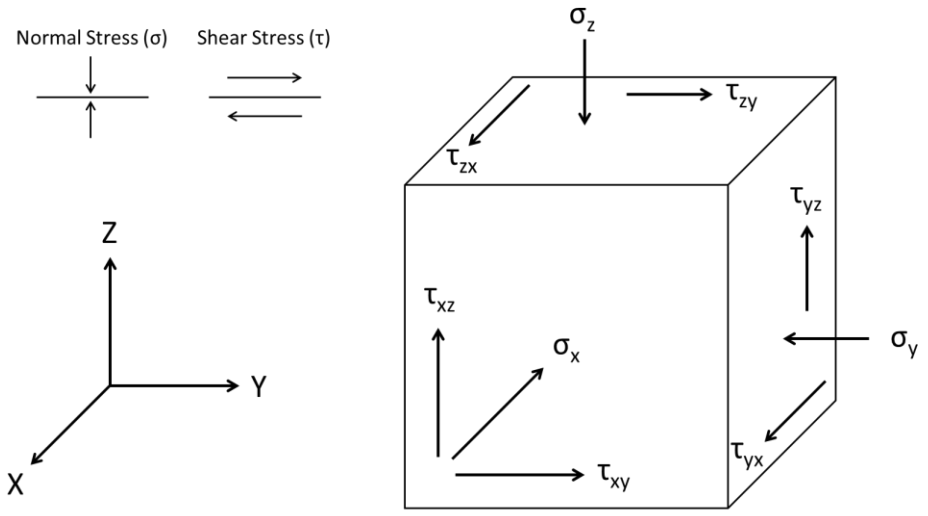

Figure 2.2: 3D stresses on a cube with respect to its axis. The normal stress (σ) is perpendicular to the axis plane while the shear stress (τ) is parallel to the axis plane.

$$\begin{bmatrix} \sigma_x & \tau_{xy} & \tau_{xz} \\ \tau_{yx} & \sigma_y & \tau_{yz} \\ \tau_{zx} & \tau_{zy} & \sigma_z \end{bmatrix} \tag{2.4}$$

If the rock (body) is considered to be in equilibrium (no translational or rotational forces acting on it), the stress tensor (Equation 2.4) simplifies down such that there are still three normal stress components, but the six shear components simplify down to three components since the shear stresses are opposite of one another must be equal in magnitude ($\tau_{xy} = \tau_{yx}$). This stress tensor is shown in Equation 2.5. The result of this is that now the stresses of a body in equilibrium can be described using three normal and three shear stresses.

$$\begin{bmatrix} \sigma_x & \tau_{xy} & \tau_{xz} \\ \tau_{yx} & \sigma_y & \tau_{yz} \\ \tau_{zx} & \tau_{zy} & \sigma_z \end{bmatrix} in\ which\ \tau_{xy} = \tau_{yx}, \tau_{xz} = \tau_{zx}, \& \tau_{yz} = \tau_{zy} \tag{2.5}$$

$$=> \begin{bmatrix} \sigma_x & \tau_{xy} & \tau_{xz} \\ \tau_{xy} & \sigma_y & \tau_{yz} \\ \tau_{xz} & \tau_{yz} & \sigma_z \end{bmatrix} \tag{2.6}$$

2.2.2. PRINCIPAL STRESSES

If the coordinate system is rotated such that the normal stress components of Equation 2.6 are equal to the maximum and minimum values resulting in the shear stress components being equal to zero, the normal stresses become re-defined as principal stresses as shown in Equation 2.7.

$$[\sigma] = \begin{bmatrix} \sigma_x & \tau_{xy} & \tau_{xz} \\ \tau_{xy} & \sigma_y & \tau_{yz} \\ \tau_{xz} & \tau_{yz} & \sigma_z \end{bmatrix} \rightarrow \begin{bmatrix} \sigma_1 & 0 & 0 \\ 0 & \sigma_2 & 0 \\ 0 & 0 & \sigma_3 \end{bmatrix} = \begin{bmatrix} \sigma_v & 0 & 0 \\ 0 & \sigma_H & 0 \\ 0 & 0 & \sigma_h \end{bmatrix} \tag{2.7}$$

Any stress field, in equilibrium, can then be defined with three orthogonal principal stresses where no shear stresses will occur. These stresses will be referred to as the in-situ stresses. Assuming the seafloor as a free even surface not translating any shear stresses, the in-situ stresses are represented by the overburden stress in the vertical direction (σ_v) and the maximum and minimum horizontal stresses (σ_H and σ_h respectively) which are orthogonal to the overburden. Given the three in-situ stresses, there are three stress regimes related to the magnitude of the in-situ stresses (Anderson, 1951).

i. Normal Faulting: $\sigma_v > \sigma_H > \sigma_h$

ii. Strike-Slip Faulting: $\sigma_H > \sigma_v > \sigma_h$

iii. Reverse Faulting: $\sigma_H > \sigma_h > \sigma_v$

2.2.3. IN-SITU PRINCIPAL STRESS MAGNITUDES

Many different methods can be used to determine the in-situ stresses for a given region depending on the stress regimes. For a normal faulting regime, empirical correlations have been developed and state that if the overburden stress is determined, the maximum and horizontal stresses are ratios of the overburden stress (Finkbeiner et al., 1996). Calculating the overburden stress can be done using the following equation:

$$\sigma_v = \int_0^D \rho(z) g dz \tag{2.8}$$

Where σ_v is the overburden stress, $\rho(z)$ is the bulk density of the formation at a depth (z), g is the acceleration due to gravity, and dz is the depth increment. An important note is that for offshore wells, the water density will replace the bulk density in the water column and needs to be included.

To determine the overburden stress with Equation 2.8, the exact formation depths and the bulk density of the formations from log data is required. For this work, regional overburden gradients are used from published sources based on well log data and are presented in Chapter 3.2.2.

2.2.4. EFFECTIVE STRESS

Sedimentary rocks encountered in oil and gas fields are porous rocks filled with connate fluids or hydrocarbons. Hardened cement is similar to rocks in that it is also a porous material (Saint-Marc et al., 2008). Porous materials often contain a fluid within the pore spaces thus creating

a pore pressure which can offset the in-situ stresses. This new stress is called the effective stress (σ') and is represented in Equation 2.9. As shown in Equation 2.9, the effective stress is related to the compressional in-situ stresses (σ) and pore pressure (P_p).

$$\sigma' = \sigma - Pp \tag{2.9}$$

In the above equation, the pore volume fluid is assumed to have negligible compressibility when compared to the compressibility of the material. The importance of this concept is that an increased pore pressure will shift the effective stresses closer to the tensile range which may be sufficient enough to cause the rock (or cement) to fail (Terzaghi, 1936; Terzaghi, 1951). A more general definition of effective stress includes Biot's coefficient (α, where $0 \leq \alpha \leq 1$) which takes into consideration for the bulk rock and grain compressibility of the material and is shown in Equation 2.10.

$$\sigma' = \sigma - \alpha Pp \tag{2.10}$$

Equation 2.10 represents the generalized effective stress model. In this work the Biot's coefficient is assumed to be one for both cement and rock materials thus reducing the effective stress model down as given in Equation 2.9.

2.2.5. STRAIN

The strain of a body is related to the resulting displacement caused by the force applied to it. The definition of strain is shown in Equation 2.11 and states that the strain (ε, unitless) is equal to the change in length (ΔL) divided by the original length (L).

$$\epsilon = \frac{L - L'}{L} = -\frac{\Delta L}{L} \tag{2.11}$$

Stress and strain are related through the theory of linear elasticity in which the relationship between the applied stresses and the resulting strains in a linear relationship which is shown in Hooke's Law in Equation 2.12.

$$\epsilon_x = \frac{1}{E}\sigma_x \tag{2.12}$$

The Poisson's ratio is the measure of lateral expansion relative to the longitudinal contraction as shown in Equation 2.13.

$$\nu = -\frac{\epsilon_y}{\epsilon_x} \tag{2.13}$$

2.2.6. WELLBORE STRESS DISTRIBUTION

When a well is drilled, the in-situ stresses in the rock are altered around the wellbore. The in-situ stresses of the wellbore are removed and replaced by a fluid column which exerts a hydrostatic pressure on the wellbore. Since the fluid pressure is different in magnitude and is now a cylindrical surface pressure instead of a combination of orthogonal stresses, a stress concentration is created around the wellbore. There are two types of stress categories:

- The in-situ stresses of the rock
- The stress concentration around the wellbore

The Kirsch (1898) equations describes the concentration of stresses for a circular hole in an infinite linear elastic plate with a uniform tension within the solid and were later modified to include anisotropic horizontal stresses and the wellbore fluid pressure (Hiramatsu and Oka, 1968; Bradley, 1979).

For the case studies in this thesis, the wellbores are oriented vertically and are parallel to the overburden stress. This assumption simplifies the Kirsch equations as illustrated in Figure 2.3.

The following Equations, 2.14 - 2.18, describe the stress concentrations around the wellbore in terms of the hoop stress (σ_θ), radial stress (σ_r), vertical stress (σ_v or σ_z), and shear stresses ($\tau_{r\theta}$, $\tau_{\theta z}$, & τ_{rz}) given the far field stresses (σ_v, σ_H & σ_h) are known.

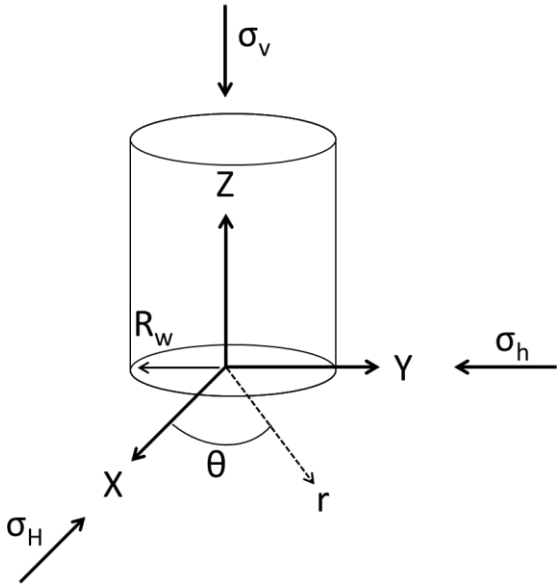

Figure 2.3: Schematic of a wellbore orientated such that the borehole is parallel to the overburden stress (σ_v).

$$\sigma_r = \frac{\sigma_H + \sigma_h}{2}\left(1 - \frac{R_w^2}{r^2}\right) + \frac{\sigma_H - \sigma_h}{2}\left(1 + 3\frac{R_w^4}{r^4} - 4\frac{R_w^2}{r^2}\right)cos2\theta + P_w\frac{R_w^2}{r^2} \tag{2.14}$$

$$\sigma_\theta = \frac{\sigma_H + \sigma_h}{2}\left(1 + \frac{R_w^2}{r^2}\right) - \frac{\sigma_H - \sigma_h}{2}\left(1 + 3\frac{R_w^4}{r^4}\right)cos2\theta - P_w\frac{R_w^2}{r^2} \tag{2.15}$$

$$\sigma_z = \sigma_v - 2v(\sigma_H - \sigma_h)\frac{R_w^2}{r^2}cos2\theta \tag{2.16}$$

$$\tau_{r\theta} = -\frac{\sigma_H - \sigma_h}{2}\left(1 - 3\frac{R_w^4}{r^4} + 2\frac{R_w^2}{r^2}\right)sin2\theta \tag{2.17}$$

$$\tau_{rz} = \tau_{\theta z} = 0 \tag{2.18}$$

At the borehole wall (with a borehole pressure, P_w):

$$\sigma_r = P_w \tag{2.19}$$

$$\sigma_\theta = \sigma_H + \sigma_h - 2(\sigma_H - \sigma_h)cos2\theta - P_w \tag{2.20}$$

$$\sigma_z = \sigma_v - 2v(\sigma_H - \sigma_h)cos2\theta \tag{2.21}$$

$$\tau_{r\theta} = \tau_{\theta z} = \tau_{rz} = 0 \tag{2.22}$$

Equation 2.20 indicates that the maximum and minimum hoop stresses at the wellbore wall will occur at:

$$\sigma_{\theta,max} = 3\sigma_H - \sigma_h - P_w \tag{2.23}$$

$$\sigma_{\theta,min} = 3\sigma_h - \sigma_H - P_w \tag{2.24}$$

in which the maximum hoop stress occurs in the direction of the minimum horizontal stress ($\theta = 90°$) and the minimum hoop stress occurs in the direction of the maximum horizontal stress ($\theta = 0$ °) as shown in Figure 2.4.

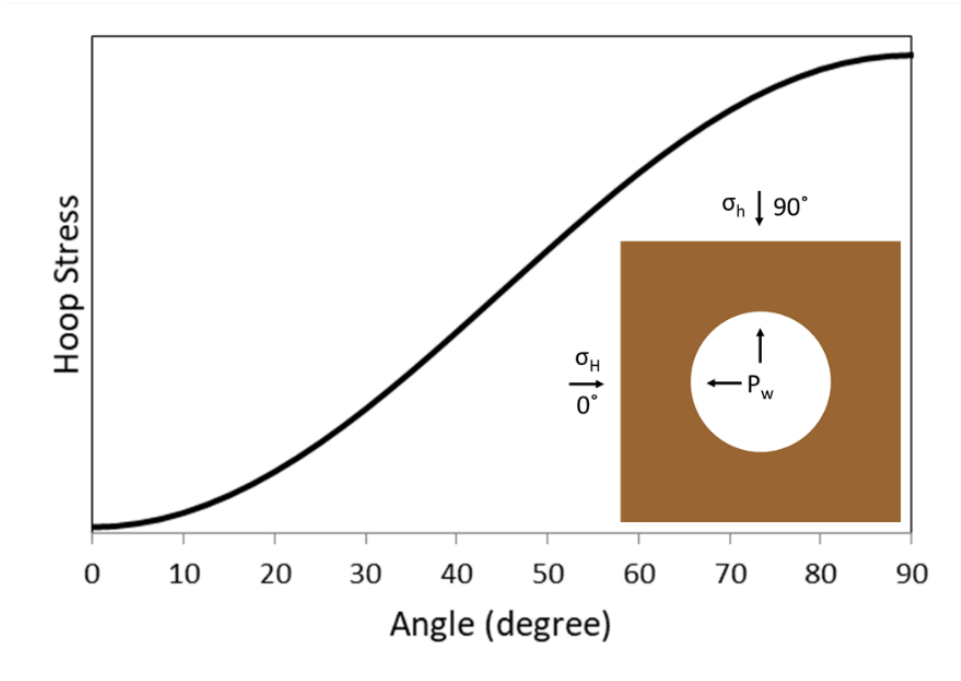

Figure 2.4: Illustration showing the magnitude of hoop stress around a wellbore.

Equations 2.14-2.17 can be converted to effective stress by taking into account the initial pore pressure (P_p).

$$\sigma'_r = \frac{\sigma_H + \sigma_h}{2}\left(1 - \frac{R_w^2}{r^2}\right) + \frac{\sigma_H - \sigma_h}{2}\left(1 + 3\frac{R_w^4}{r^4} - 4\frac{R_w^2}{r^2}\right)cos2\theta + (P_w - P_p)\frac{R_w^2}{r^2} \tag{2.25}$$

$$\sigma'_\theta = \frac{\sigma_H + \sigma_h}{2}\left(1 + \frac{R_w^2}{r^2}\right) - \frac{\sigma_H - \sigma_h}{2}\left(1 + 3\frac{R_w^4}{r^4}\right)cos2\theta - (P_w - P_p)\frac{R_w^2}{r^2} \tag{2.26}$$

$$\sigma'_z = \sigma_v - 2v(\sigma_H - \sigma_h)\frac{R_w^2}{r^2}cos2\theta - P_p \tag{2.27}$$

$$\tau'_{r\theta} = -\frac{\sigma_H - \sigma_h}{2}\left(1 - 3\frac{R_w^4}{r^4} + 2\frac{R_w^2}{r^2}\right)sin2\theta - P_p \tag{2.28}$$

And Equations 2.19-2.21 and ultimately Equations 2.23 & 2.24 respectively:

$$\sigma'_r = P_w - P_p \tag{2.29}$$

$$\sigma'_\theta = \sigma_H + \sigma_h - 2(\sigma_H - \sigma_h)cos2\theta - P_w - P_p \tag{2.30}$$

$$\sigma'_z = \sigma_v - 2v(\sigma_H - \sigma_h)cos2\theta - P_p \tag{2.31}$$

With a max and min of:

$$\sigma'_{\theta,max} = 3\sigma_H - \sigma_h - P_w - P_p \tag{2.32}$$

$$\sigma'_{\theta,min} = 3\sigma_h - \sigma_H - P_w - P_p \tag{2.33}$$

According to the Kirsch analytical equations for anisotropic poro-elastic material with a pressurized open hole, the plot of effective hoop and radial stresses versus the ratio of the position, r, to the wellbore radius, R_w, shows that the stress concentrations around the open hole dissipate into the in-situ stresses within ten wellbore radii as illustrated in Figure 2.5. The ten wellbore radii

for the boundary conditions is fundamental with numerical simulations to ensure the boundary conditions do not affect the wellbore stress concentration.

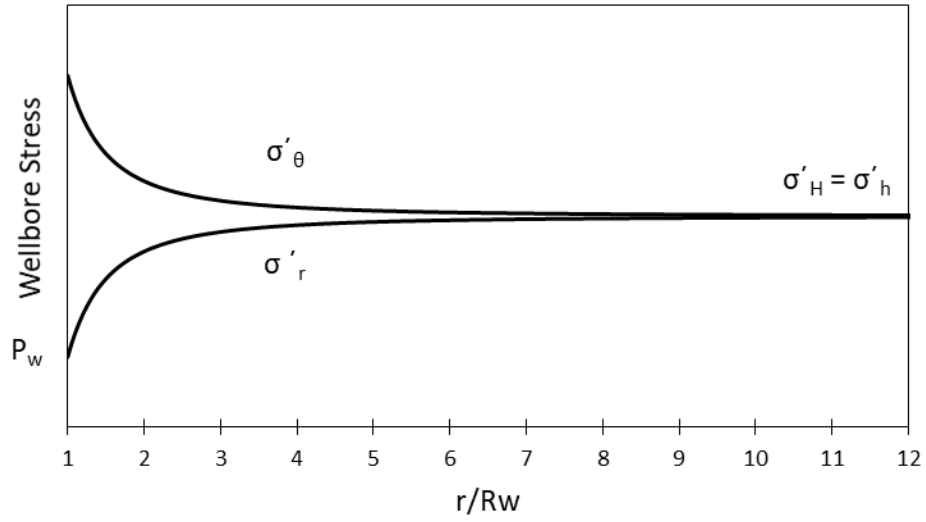

Figure 2.5: Kirsch analytical solution of the effective hoop and radial stress from the wellbore versus the distance away from the wellbore. The effective hoop and radial stress converge to the effective in-situ stresses (σ'_H& σ'_h) at a ratio of 10 wellbore radii away from the wellbore wall.

2.3. FAILURE OF ROCK AND CEMENT

2.3.1. SHEAR FAILURE IN CEMENT AND ROCK

The most common failure criteria used in geomechanics is Mohr-Coulomb, and it is used to determine when shear failure will occur. This theory states that the failure of material is due to the combination of normal and shear stresses. The normal and shear stresses are determined by only the minimum (σ_3) and maximum (σ_1) principal stresses. The failure line is given by Equation 2.34.

$$\tau_f = \tau_o + \sigma' \tan(\phi) = \tau_o + \sigma' \mu \tag{2.34}$$

Where τ_f = shear strength, τ_o = cohesion, ϕ = internal friction angle, μ = coefficient of internal friction, and σ' = effective normal stress.

The normal and shear effective stresses that cause the failure within the rock are given by Equations 2.35 & 2.36, respectively, and illustrated in Figure 2.6.

$$\sigma' = \frac{1}{2}(\sigma_1' + \sigma_3') + \frac{1}{2}(\sigma_1' - \sigma_3')cos2\beta \tag{2.35}$$

$$\tau' = \frac{1}{2}(\sigma_1' - \sigma_3')sin2\beta \tag{2.36}$$

The rock is in shear failure if (σ', τ') touches or crosses the failure line, τ_f. The rock is in tensile failure if (σ', τ') touches or crosses the shear (τ') axis. The concept of shear and tensile failure is illustrated in Figure 2.7.

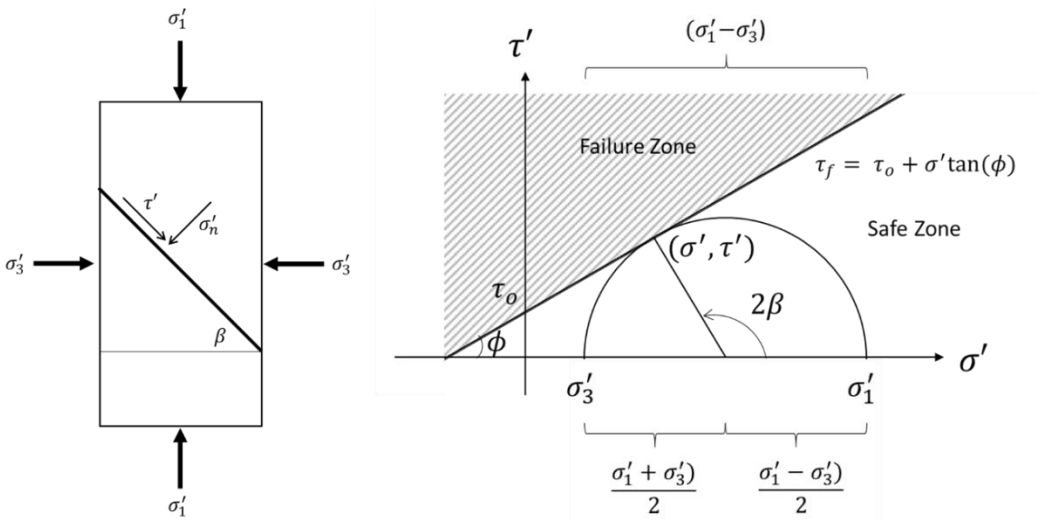

Figure 2.6: A) Mohr-Coulomb failure criteria of a cylindrical sample. B) Mohr circle depicting the failure criteria.

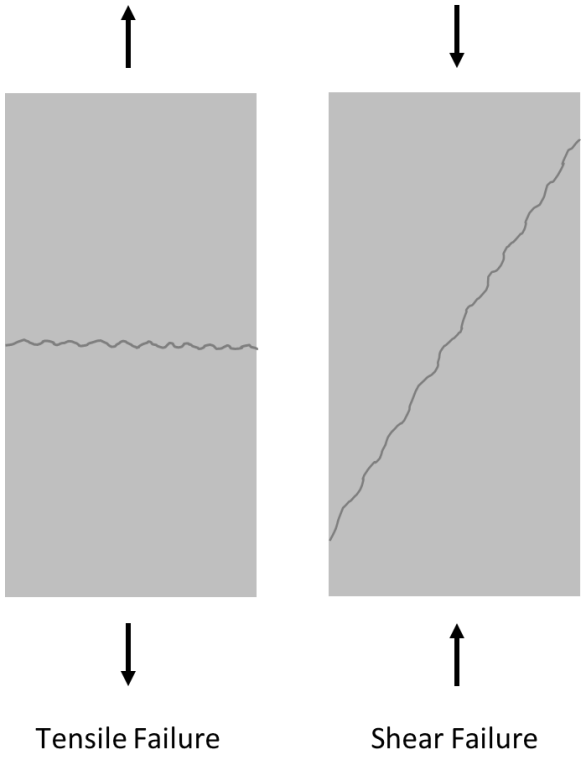

Figure 2.7: Illustration showing tensile and shear failure.

2.3.2. CEMENT SHEATH FAILURE MECHANISMS

A cement sheath can have multiple failure mechanisms in which hydrocarbon leakage may occur. As described by Bois et al. (2011), important failure mechanisms include inner debonding, outer debonding, radial cracks, shear cracks, and disking. For the analysis in this thesis, the failure criteria are defined as follows. Inner and outer debonding occur at the casing/cement and cement/rock formation interfaces, respectively, when the effective radial stress is in tensile as shown in Equation 2.42. Radial cracks occur when the effective hoop stress is less than the tensile strength of the cement as shown in Equation 2.43. Shear cracks occur when the effective shear stress is greater than the maximum allowable shear stress of the cement (as defined by Mohr-Coulomb failure criteria) as shown in Equation 2.44. Disking occurs when the effective vertical stress is less than the tensile strength of the cement as shown in Equation 2.45. A schematic of these failure mechanisms is illustrated in Figure 2.8.

$$\sigma_r' \leq 0 \quad \text{(Debonding)} \tag{2.42}$$

$$\sigma_\theta' \leq T_o \quad \text{(Radial Cracks)} \tag{2.43}$$

$$\tau_f \geq \tau_{Mohr-Coulomb} \quad \text{(Shear Cracks)} \tag{2.44}$$

$$\sigma_\theta' \leq T_o \quad \text{(Disking)} \tag{2.45}$$

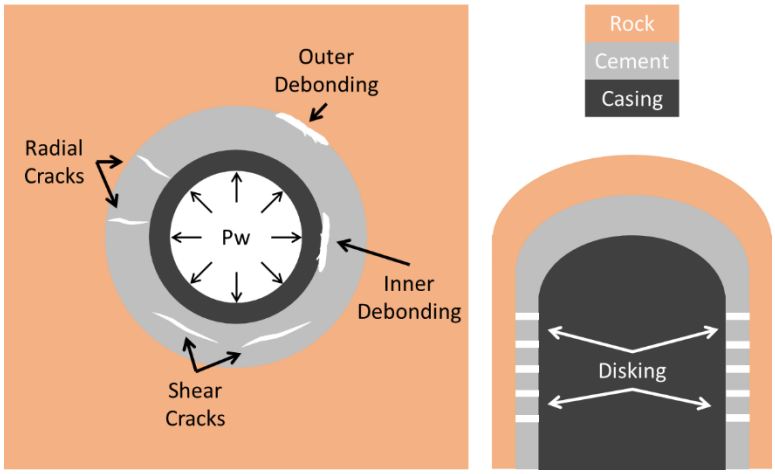

Figure 2.8 A: Failure mechanisms within the cement sheath showing inner and outer debonding, radial cracks, and shear cracks. B: Failure mechanism within the cement sheath showing disking.

2.4. MODELING

2.4.1. CEMENT SHEATH ANALYTICAL VERIFICATION

An analytical model of the stress distribution around the wellbore can be developed using thick-walled cylinder equations and the Kirsch solution described in Chapter 2.2.6. Figure 2.9 depicts a model sketch for a cased wellbore with its general dimensions used in the analytical model. The thick-walled cylinder equations are described by Weideman (2014).

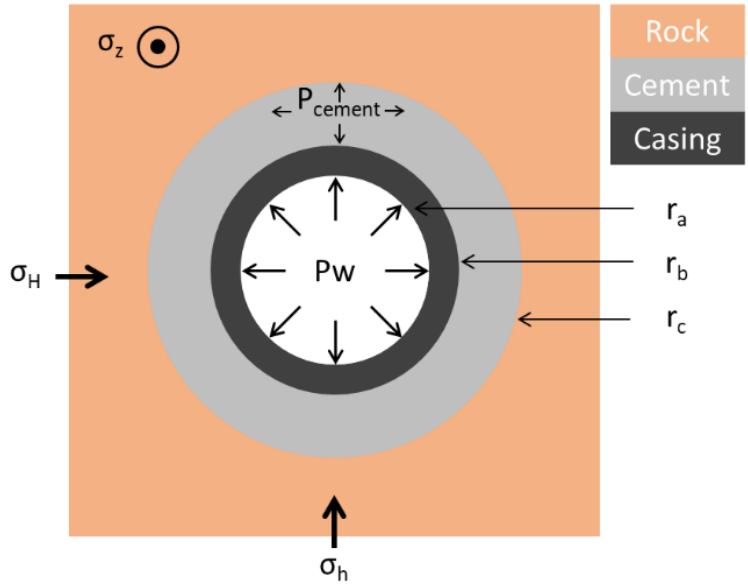

Figure 2.9: Wellbore sketch showing generalized radii of the three bodies used in the analytical stress distribution equations.

Starting from the center of the wellbore outwards, the stress distributions in the casing are determined from a single thick-walled cylinder. It is important to note that all the equations presented in this section are effective stresses. In the case of the casing, a generalized effective stress equation for a thick-walled cylinder is presented in Equations 2.46, 2.47, and 2.48 to represent the radial, hoop, and axial stresses, respectively. It is also assumed that the radial stress of the hardened cement or hydrostatic pressure of the cement slurry (P_{cement}) is known. If the stress of the cement is unknown, more complex analytical equations are required that include the stress-strain relationship of the materials (E and υ).

$$\sigma'_{r_{casing}} = \frac{r_b^2\, P_{cement} + r_a^2\, P_w}{r_b^2 - r_a^2} + \frac{r_a^2\, r_b^2\, (P_w - P_{cement})}{(r_b^2 - r_a^2) r^2} - P_{p_{casing}} \tag{2.46}$$

$$\sigma'_{\theta_{casing}} = \frac{r_b^2\, P_{cement} + r_a^2\, P_w}{r_b^2 - r_a^2} - \frac{r_a^2\, r_b^2\, (P_w - P_{cement})}{(r_b^2 - r_a^2) r^2} - P_{p_{casing}} \tag{2.47}$$

$$\sigma'_{z_{casing}} = \sigma_{v_{casing}} - P_{p_{casing}} \tag{2.48}$$

The general equation to calculate the overburden stress is a function of the material density and the height of the material as shown in Equation 2.49 (and discussed previously in Chapter 2.2.3.

$$\sigma_v = \int_0^z \rho(z) g \, dz \tag{2.49}$$

Steel is assumed to have zero pore pressure thus Equations 2.46, 2.47, and 2.48 will simplify down to Equations 2.50, 2.51, and 2.52.

$$\sigma'_{r_{casing}} = \frac{r_b^2 \, P_{cement} + r_a^2 \, P_w}{r_b^2 - r_a^2} + \frac{r_a^2 \, r_b^2 \, (P_w - P_{cement})}{(r_b^2 - r_a^2) r^2} \tag{2.50}$$

$$\sigma'_{\theta_{casing}} = \frac{r_b^2 \, P_{cement} + r_a^2 \, P_w}{r_b^2 - r_a^2} - \frac{r_a^2 \, r_b^2 \, (P_w - P_{cement})}{(r_b^2 - r_a^2) r^2} \tag{2.51}$$

$$\sigma'_{z_{casing}} = \sigma_{v_{casing}} \tag{2.52}$$

The cement sheath stresses are calculated using the same procedure as the casing. The equations that represent the radial, hoop, and axial stresses are given in Equations 2.53, 2.54, and 2.55.

$$\sigma'_{r_{cement}} = \frac{r_c^2 \, P_{cement\ at\ c} + r_b^2 \, P_{cement\ at\ b}}{r_c^2 - r_b^2} + \frac{r_b^2 \, r_c^2 \, (P_{cement\ at\ b} - P_{cement\ at\ c})}{(r_c^2 - r_b^2) r^2} - P_{p_{cement}} \tag{2.53}$$

$$\sigma'_{\theta_{cement}} = \frac{r_c^2 \, P_{cement\ at\ c} + r_b^2 \, P_{cement\ at\ b}}{r_c^2 - r_b^2} - \frac{r_b^2 \, r_c^2 \, (P_{cement\ at\ b} - P_{cement\ at\ c})}{(r_c^2 - r_b^2) r^2} - P_{p_{cement}} \tag{2.54}$$

$$\sigma'_{z_{cement}} = \sigma_{v_{cement}} - P_{p_{cement}} \tag{2.55}$$

For the scenario assumed in this thesis, the cement stress exerts constant radial stress at both the casing/cement and cement/rock interface. Therefore, $P_{cement\ at\ b} = P_{cement\ at\ c}$ resulting in the second term falling out of Equations 2.53 and 2.54 which in turn resulting in constant radial and hoop stress throughout the cement sheath as shown in Equations 2.56 and 2.57.

$$\sigma'_{r_{cement}} = \frac{r_c^2\ P_{cement}\ +\ r_b^2\ P_{cement}}{r_c^2 - r_b^2} - P_{p_{cement}} \tag{2.56}$$

$$\sigma'_{\theta_{cement}} = \frac{r_c^2\ P_{cement}\ +\ r_b^2\ P_{cement}}{r_c^2 - r_b^2} - P_{p_{cement}} \tag{2.57}$$

Equations 2.58, 2.59, 2.60, and 2.61 are modified from the Kirsch analytical solutions described in Chapter 2.2.6 to show the radial, hoop, axial, and shear stress relationship in the rock formation between the far-field stresses, initial pore pressure, and stress from the cement.

$$\sigma'_{r_{rock}} = \frac{1}{2}(\sigma_H + \sigma_h - 2P_{p_{rock}})\left[1 - \left(\frac{r_c}{r}\right)^2\right] + \frac{1}{2}(\sigma_H - \sigma_h)\left[1 - 4\left(\frac{r_c}{r}\right)^2 + 3\left(\frac{r_c}{r}\right)^4\right] cos2\theta + (P_{cement} - P_{p_{cement}})\left(\frac{r_c}{r}\right)^2 \tag{2.58}$$

$$\sigma'_{\theta_{rock}} = \frac{1}{2}(\sigma_H + \sigma_h - 2P_{p_{rock}})\left[1 - \left(\frac{r_c}{r}\right)^2\right] - \frac{1}{2}(\sigma_H - \sigma_h)\left[1 + 3\left(\frac{r_c}{r}\right)^4\right] cos2\theta - (P_{cement} - P_{p_{cement}})\left(\frac{r_c}{r}\right)^2 \tag{2.59}$$

$$\sigma'_{z_{rock}} = \sigma_v - 2\upsilon(\sigma_H - \sigma_h)\left(\frac{r_c}{r}\right)^2 cos2\theta\ -\ P_{p_{rock}} \tag{2.60}$$

$$\tau'_{r\theta} = -\frac{\sigma_H - \sigma_h}{2}\left(1 - 3\left(\frac{r_c}{r}\right)^4 + 2\left(\frac{r_c}{r}\right)^2\right) sin2\theta - P_{p_{rock}} \tag{2.61}$$

Equations 2.50, 2.51, 2.56, 2.57, 2.58, and 2.59 are used to determine the analytical solutions of the radial and hoop stress development along a radius of interest within a wellbore.

2.4.2. WELLBORE INTEGRITY FINITE ELEMENT ANALYSIS

The analytical model discussed in the previous section lacks complexity to accurately represent complex geometries (such as non-concentric wellbores), complicated boundary conditions, and complex failure analysis such as fracture mechanics and debonding mechanisms (Salehi and Nygaard, 2015). To address these shortcomings, finite element models have become an important tool to study the creation and severity of leakage pathways in cement sheaths for over 20 years.

Bosma et al. (1999) used a 2D-FEA to evaluate different forms of cement failure as a thermos-elasto-plastic model with Mohr-Coulomb plasticity to describe shear failure, and smeared cracking to determine debonding. A major conclusion of their work is that the failure of the cement sheath is dependent on the initial stress within the sheath such that if an initial stress in the cement is present, shear failure and debonding were predominate failure mechanisms. Previous cement integrity analysis used compressive strength as the only indicator for cement integrity, and their research determined that the compressive strength is not sufficient for determining the ability of the cement to provide a seal. Bosma et al. (1999) determined other mechanical properties should be evaluated such as Young's modulus, Poisson's ratio, tensile strength, shear strength, bonding strength, and cement shrinkage and expansion. A significant limitation of their work is that they did not consider the porous nature of the cement and rock formation.

Fleckenstein et al. (2001) performed linear elastic 2D FEA in which they evaluated von-Mises stresses for cement sheath failure, but their work also failed to evaluate the cement and rock formation as a poro-elastic material. Fleckenstein et al. determined that the primary failure mechanism of cement sheath failure is radial cracking due to tensile, tangential stresses (tensile hoop stresses). The tangential stresses are reduced with ductile cement compositions that have higher Poisson's ratios and lower values of Young's modulus. Brittle cement compositions tend to develop greater tensile tangential stresses resulting in greater cement failure (cracking).

Ravi et al. (2002) extended Bosma et al.'s (1999) 2D elasto-plastic model by performing staged simulations to represent the drilling of a wellbore, completion of the well, and production of the well. The same failure modes were analyzed as with Bosma et al.'s (1999) model, except Ravi et al. (2002) also included cement shrinkage and expansion parameters. Ravi et al. (2002) determined that the integrity of the cement sheath is controlled by its mechanical properties, formation properties, and well operating parameters. Pattillo and Kristiansen (2002) implemented a staged 2D elasto-plastic FEA approach to investigate tubular failure based off Drucker-Prager criteria in horizontal wellbores with imperfect cementing placement. Their simulation stages included the history of the formation from discovery in-situ stresses, global pore pressure depletion for the field, addition of the wellbore to the formation, and local production. The goal of their study was to investigate how the changes in vertical stresses affect horizontal wellbore failure. A limitation of Pattillo and Kristiansen's (2002) 2D approach is that anisotropic stresses were not included. Only the vertical and one horizontal stress were analyzed due to the 2D nature of horizontal wellbores.

Gray et al. (2009) established a framework for a 3D elasto-plastic life-of-well FEA to evaluate cement debonding (based off contact bond strength) and failure (based off Mohr-Coulomb criterion) at all stages of a wellbore after construction. Their model included far-field stresses, cement hardening and shrinkage, and debonding at the casing/cement and cement/formation interfaces. Nygaard et al. (2014) and Weideman and Nygaard (2014) expanded Gray et al.'s (2009) model to include temperature changes and poroelasticity while evaluating wellbore near term and long-term integrity, cement and casing deformation (Li and Nygaard, 2017), and quantify micro-annuli widths (Bois et al., 2012; Zhang et al., 2017). The results of the expanded Gray et al. (2009) models determined that changes in wellbore pressure and temperature are predominant factors that cause cement sheath debonding, but the authors are not in agreement on which cement sheath interface is experiencing debonding. Zhang et al. (2017) concluded that debonding occurs at the

cement/rock formation interface while Nyggard et al. (2014) and Weideman and Nygaard (2014) determined debonding to occur at the casing/cement interface. Gray et al. (2009) experienced debonding at the casing/cement interface, but the authors only modeled debonding criterion at the casing/cement interface.

The studies presented in the paragraph above have either attempted to quantify which parameters are important in cement sheath failure (but ignored important cement sheath characteristics such as cement pore pressure) or focused on specific scenarios without considering variations in wellbore parameters. The purpose of this study is to develop a staged FEA 3D poroelastic model to evaluate the potential of cement sheath failure through the mechanisms described in Chapter 2.3.2 and to perform a parametric analysis to develop an understanding of which wellbore properties are have the largest impact on cement sheath integrity.

2.5. CEMENT HYDRATION

Portland cement is a powder that, when mixed with water, produces a paste that evolves with time to a solid material. Portland cement is initially made from the mixing of raw materials (such as lime, silica, and alumina) and heated to 1,500 °C to form clinker. The clinker is composed mainly of Alite, Belite, Aluminite, and Ferrite (Bensted and Barnes, 2002). The clinker is ground down to specific particle sizes and the resulting product is called Portland cement (Bensted and Barnes, 2002).

The compounds within Portland cement are anhydrous which means that they react with water. The mixing of water with Portland cement starts a complex chemical process (called cement hydration) that initially reacts quickly (minutes) and takes a long time to fully react (months to years) (Bensted and Barnes, 2002). Hydration of Portland cement creates four main components: remaining anhydrous grains (un-hydrated clinker), high-density calcium silicate hydrate (CSH), low-density CSH (which is composed of Ettringite and other impurities), and portlandite (which is

hardened calcium hydroxide) (Bensted and Barnes 2002). Cement hydration results in intergranular and intragranular porosity. The intergranular porosity is due to the volume of the end products (cement hydration products and water) are smaller than the volume of the initial reactants (Portland cement powder and water). The intragranular porosity occurs within the CSH grains (Bois et al., 2011). Since the hardened cement material has pores, they are filled with either gas or liquid resulting in a pore pressure. Saint-Marc et al. (2008) and Bois et al. (2012) determined that once cement hydration is complete, the pore pressure of the cement is equal to the cavitation pressure of the remaining water. This means that the pore pressure on hydrated cement is equal to the vaporization pressure of the water solution. If the hardened cement has access to an outside pressure, which would be available in a permeable rock formation (rock pore pressure), the pressures will "equalize" resulting in the cement pore pressure becoming equal with the surrounding pressure (Bois et al., 2011). Therefore, cement hydration in a wellbore will result in the cement pore pressure being equal to the surrounding rock formation pore pressure. The time required for the pressures to equalize is dependent on the permeability of the cement and rock formation. Low permeability systems will require longer time periods for the pressure to equalize (if at all) while high permeability systems will equalize quicker.

Modeling cement hydration in FEA is difficult since hydration consists of complex chemical reactions involving phase changes from essentially a liquid (cement slurry) to a solid (cement paste/hardened cement). For the purpose of FEA modeling, cement hydration can be broken into two categories; the cement slurry is a liquid which behaves according to fluid mechanics, and the cement paste is a solid which behaves according to poromechanics (Bois et al. 2011). When the cement is a slurry, it is pumped in the annulus between the rock and casing therefore creating a hydrostatic column that applies pressure radially to the rock and casing (Ravi et al., 2002; Gray et al., 2009; Bois et al., 2011; Weideman, 2014). Once hydration is complete and the cement is hardened, there is much debate on how the state of the stress in the cement. Ravi

et al. (2002) assumed that the stress of the set cement is dependent upon the shrinkage/expansion of the cement volume variation. Thiercelin et al. (1998), Bosma et al. (1999), Ravi et al. (2002), and Nelson and Guillot (2006) assumed that the cement is under no initial effective stress (i.e. effective stress is equal to zero). Gray et al. (2009), Bois et al. (2012), Weideman (2014), and Nygaard et al. (2014) all state that the setting stress of the cement is equal to the hydrostatic column of the cement slurry. The theory that the setting stress is equal to the hydrostatic column of the cement slurry is validated by Jackson and Murphey (1993) in which they determined experimentally that the cement sheath has a "high level" of stress once fully hydrated. For the use in this study, the cement sheath is assumed to have had enough time for the pore pressure to equalize to that of the surrounding rock formation and the setting stress of hardened cement is equal the hydrostatic column of the cement slurry.

CHAPTER III

STUDY AREA

3.1. GULF OF MEXICO

Drilling in the GoM started in the early 1900's with very primitive rigs connected to land by piers in shallow water (~20 ft.). The oil industry boomed in the GoM after the Second World War leading to two major changes: more wells were drilled, and technological advancements were made that allowed wells to be in deeper waters (BSEE.gov). The deepest wells are now drilled in 10,000 ft. of water, but the majority of wells drilled are still in shallow water (<240 ft.).

The GoM is categorized into two major groups: state owned seabed and federal owned seabed. The individual coastal states own the seabed within three miles of the individual state's coast while the Federal government owns the seabed from the three-mile mark to a line approximately 200-300 miles offshore. This area is known as the Outer Continental Shelf (OCS). All of the wells in the GoM located in the OCS are under the jurisdiction of the Bureau of Ocean Energy Management (BOEM) and their sister agency, the Bureau of Safety and Environmental Enforcement (BSEE). The BOEM manages the development of energy and mineral resources while the BSEE promotes and enforces safety in offshore energy exploration and production within the OCS.

The OCS is divided up into three regions: the Western Gulf of Mexico Planning Area, the Central Gulf of Mexico Planning Area, and the Eastern Gulf of Mexico Planning Area as illustrated in Figure 3.1. Only the Western Planning Area and the Central Planning Area have active leases at the time of this publication. The Eastern Planning Area is under a congressional moratorium, meaning that activity is not allowed at the present time. The planning areas are then subdivided into Official Projection Diagrams (OPD's) which are then divided into more grids similar to onshore townships and ranges.

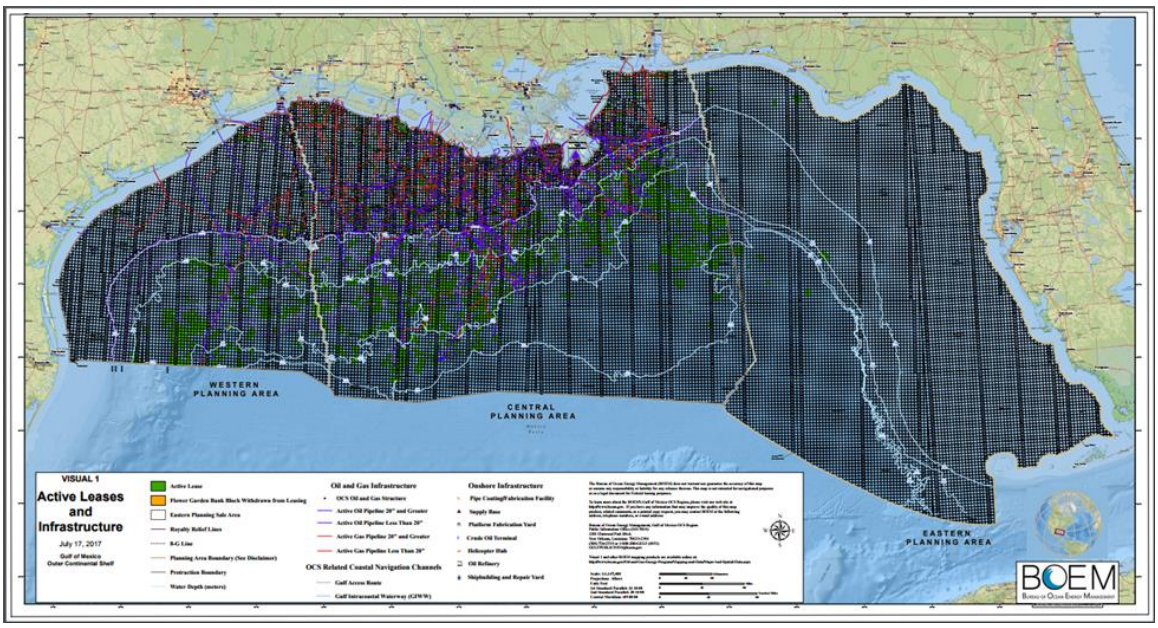

Figure 3.1: The Outer Continental Shelf (OCS) of the Gulf of Mexico showing the three planning areas: the Western Planning Area, the Central Planning Area, and the Eastern Planning Area. Figure from www.boem.gov.

As of 9/13/18, there are 54,291 wells in the OCS of the GoM. There are 31,192 abandoned wells in which 27,691 wells are permanently abandoned (PA), and 3,501 wells are temporarily abandoned (TA). The distribution of wellbore statuses in the OCS are shown in Figure 3.2.

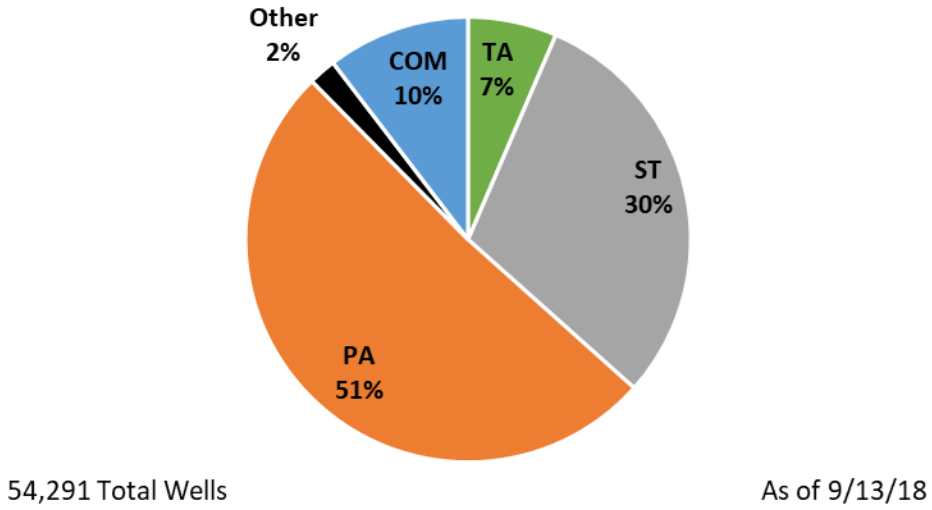

Figure 3.2: The distribution of wells in the Outer Continental Shelf (OCS) in the Gulf of Mexico. Note: TA = temporarily abandoned, PA = permanently abandoned, COM = borehole completed, ST = sidetracked wellbore, and Other = various wellbore statuses for wellbores in the planning stage.

The characteristics of wells in the OCS are described in the following figures. The general trends for wells in the OCS are that as newer wells were spud, the total true vertical depths (TVD) became deeper (Figure 3.3). The same is true for water depths (Figure 3.4). Cross-plotting the total depth versus water depth results in a relationship between the two (Figure 3.5). The deeper total depth wells are located in deeper water depths. Advancements in technology can be seen in Figure 3.6 in that most wells were drilled in less than 2,000 ft. of water before the 1990's. Then wells were being drilled in deeper water depths resulting in significantly deeper wells (in TVD).

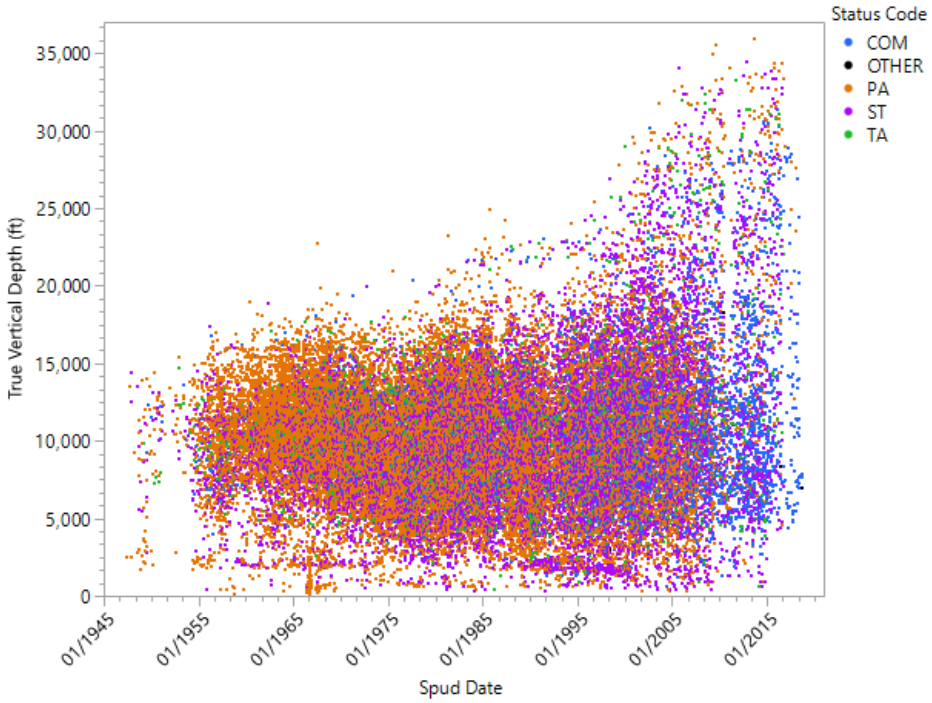

Figure 3.3: Total True vertical depth (TVD) vs. wellbore spud date with color coordinated status codes. A positive association between TVD and spud date is indicated.

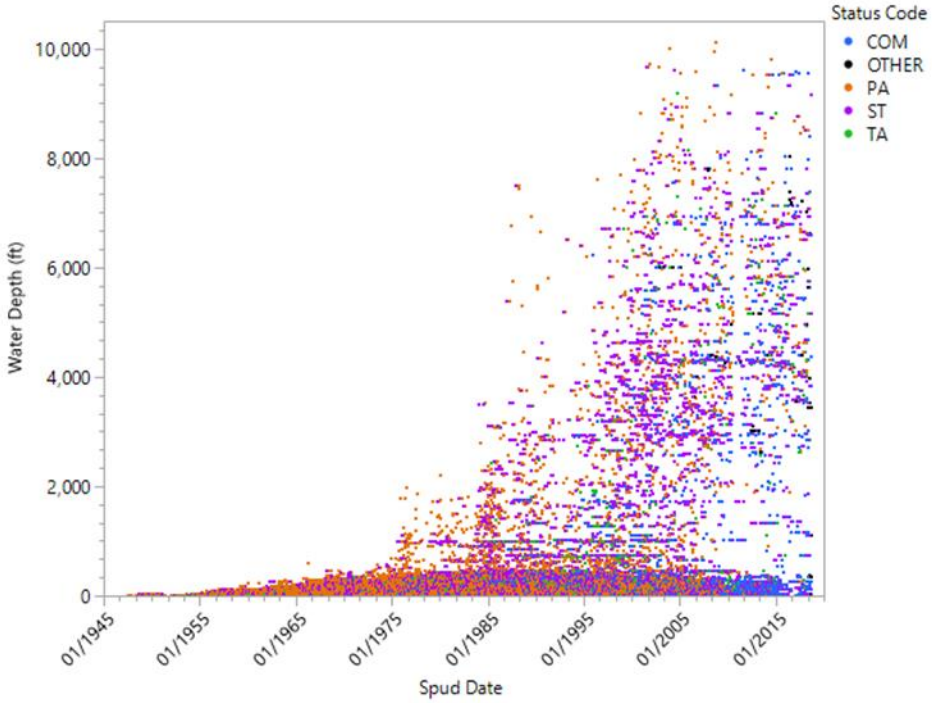

Figure 3.4: Water depth vs. wellbore spud date with color coordinated status codes. A positive association between water depth and spud date is indicated. The majority of wells drilled before 1975 were within 500 ft. of water. The newer wells were drilled up to and exceeding 10,000 ft. of water.

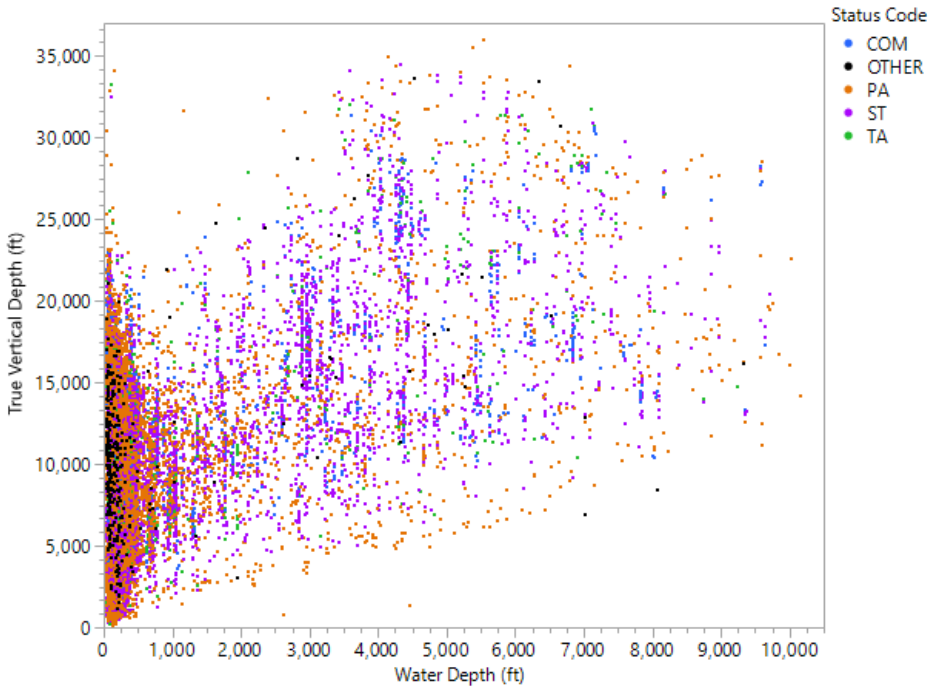

Figure 3.5: TVD vs. water depth with color coordinated status codes. A positive association between TVD and water depth is indicated. The deeper wells usually resided in deeper water depths. These wells ranged from very shallow TVD wells to wells with upwards of 35,000 ft. TVD.

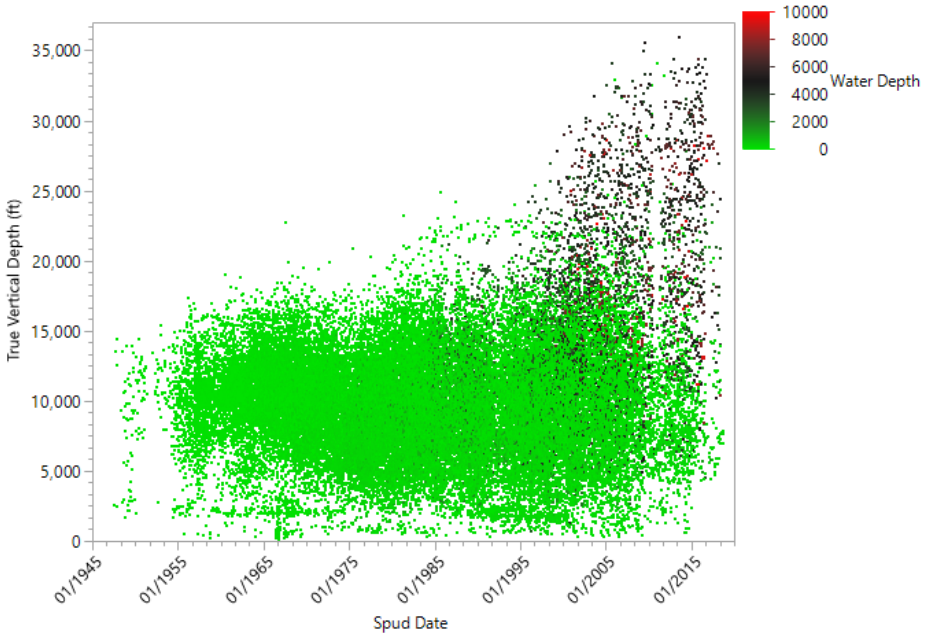

Figure 3.6: TVD vs. wellbore spud date with color indicating water depths. Technological advancements in the 1990's allowed wells to be drilled in deeper water depths resulting in deeper TVD's.

3.2. EUGENE ISLAND OPD

As previously stated, there are 54,291 wells in the OCS in the GoM. The Eugene Island OPD, located in the Central GoM planning area, was selected to represent wells with a range of ages, statuses, and depths. This will significantly reduce the number of wells needing to be analyzed, and the results will be applicable to that specific region.

In the Eugene Island OPD, there are 6,167 unique API Well Numbers according to the BSEE. Available data from BSEE include specific well names, API well identifiers, lease numbers, sea floor area, bottom block number, water depth, lease owner, spud dates, total TVD, well status, dates for well status changes, and much more information. All of the wells in the Eugene Island OPD have a status of: "Cancelled (CNL)", "Completed (COM)", "Permanently Abandoned (PA)", "Temporarily Abandoned (TA)", "Sidetracked (SI)", or "Approved Sidetrack (AST)".

Many of the wells in the OPD have been sidetracked meaning that a sidetracked well is spud off of a parent well. Sidetracked wells are considered a separate well and have a unique API number. However, sidetracked wells share the parent well's surface and intermediate casings. To avoid duplications, wells that had a status code of "ST" or "AST" were omitted from the data set. Wells that were canceled ("CNL" status) were also omitted because only wells that were completed or abandoned are of interest in this study. Omitting those wells lowered the number of unique wells from 6,167 to 4,030. The distribution of wells before and after omission are shown in Figure 3.7. As indicated in Figure 3.7, the average well in the Eugene Island OPD has a status of permanently abandoned.

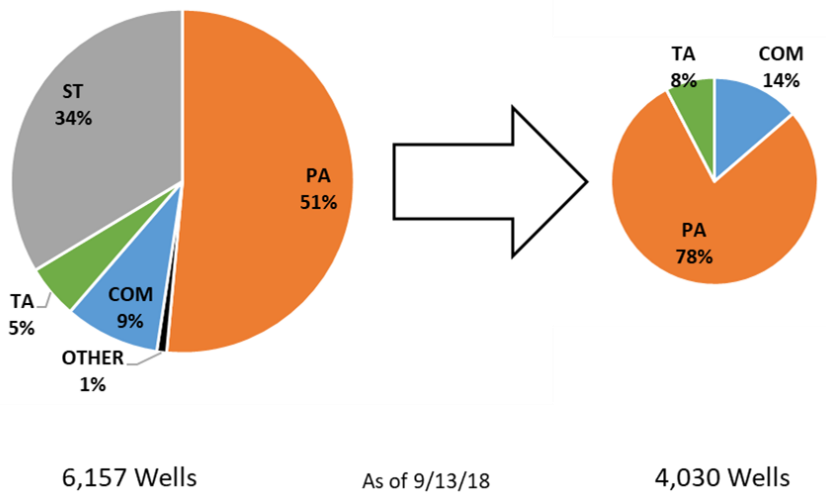

Figure 3.7: The distribution of wells from the Eugene Island OPD before and after removing 2,127 wells that had a status of CNL, ST, and AST.

The distribution of the total TVD of the wells in the Eugene Island OPD are shown in Figure 3.8. The wells range from a non-zero depth[1] of 245 ft. to 34,162 ft. The average TVD is 9,808 ft. with a standard deviation of 3,604 ft. Figure 3.8 indicates that most of the wells that are still producing (status code of completed) have a medium range TVD of between 4,000 – 12,000 ft.

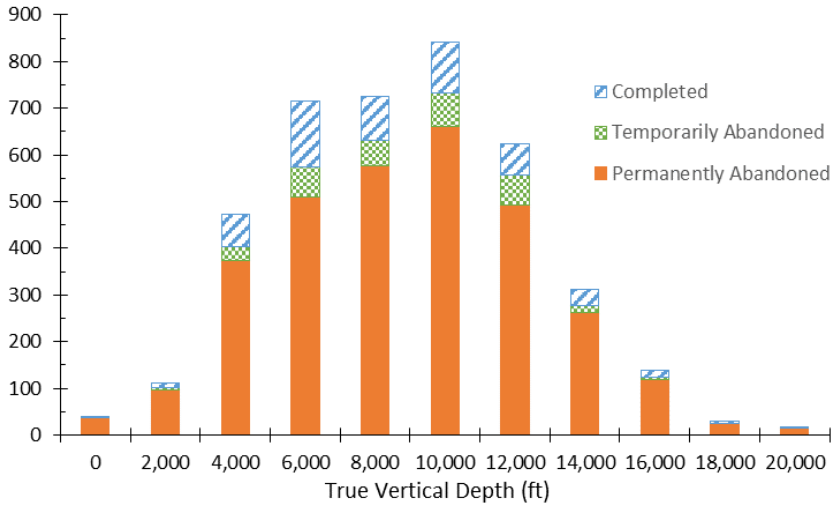

Figure 3.8: TVD distribution of the wells in the Eugene Island OPD including the distribution of their respective status codes of Completed (COM), Temporarily Abandoned (TA), or Permanently Abandoned (PA).

[1] Some wells had a depth of 0 ft. This is due to a lack of complete records in which the TVD was not known.

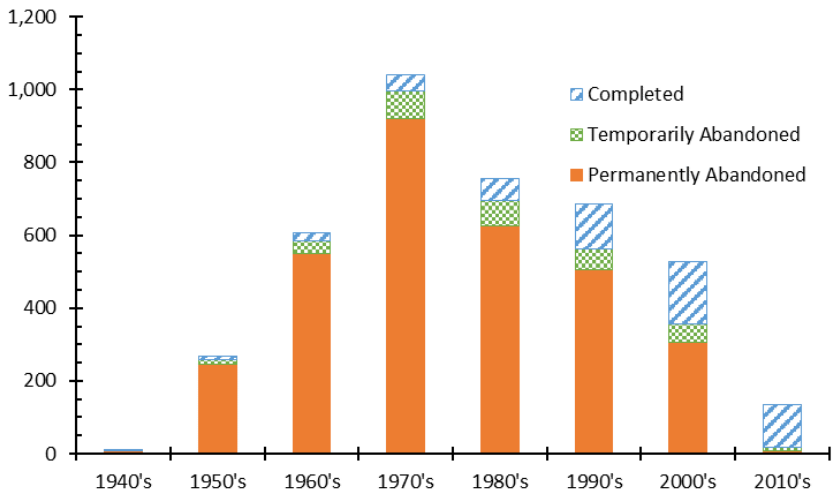

Figure 3.9: Spud date distribution of the wells in the Eugene Island OPD including the distribution of their respective status codes of COM, TA, or PA.

The distribution of borehole spud dates with their respective status codes is shown in Figure 3.9. The first borehole spud in the Eugene Island OPD was May 1947, and the most recent borehole was spud in June 2018. It is important to note that active drilling is still occurring in this OPD, and the data used in this project was acquired in September 2018. The average borehole spud date is 07/06/1982 with a standard deviation of 15.3 years. Figure 3.9 shows that the majority of the wells that are still producing are recently drilled (within the last three decades). It is interesting to note that 13% of the 135 wells drilled after 2010 are abandoned (9 TA & 9 PA).

As shown in the previous figure, most of the wells drilled in any decade (except for the most recent one) are abandoned (either temporarily or permanently). Figure 3.10 shows when these wells had their status change versus when they were spud. The earliest a well can have its status change is when it was drilled (spud date) as shown by the line in Figure 3.10. The individual wells are color-coded based on their status. COM wells are blue, PA wells are orange, and TA wells are green. There is an obvious cluster of green data points towards the top of the figure. That indicates that a lot of older wells have recently had their status changed to TA. Another trend indicates that many older wells have recently been PA (from 2005 to present). Due to the increase in well abandonment, the need to determine enhanced cement qualities to prevent leakage is critical.

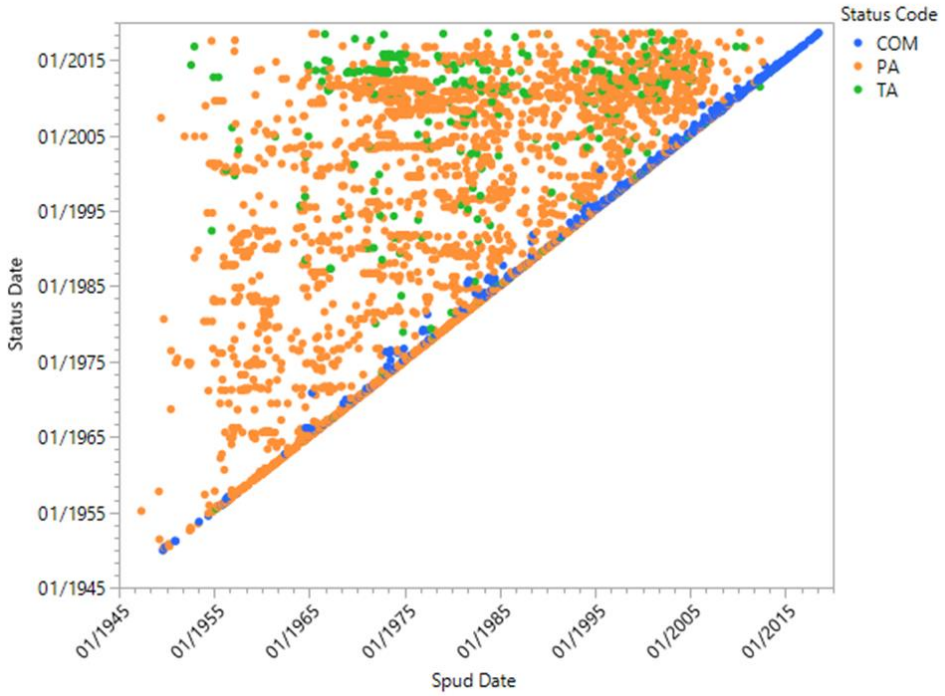

Figure 3.10: Spud date vs. status change date of wells color coordinated by their status code. An increase in abandonment of older wells is shown by the cluster of data points the status change dates 2005-present.

The distribution of well water depths with their respective status codes is shown in Figure 3.11. The range of non-zero water depths are from 8 ft. to 550 ft. The average water depth is 151 ft. with a standard deviation of 105 ft. It is important to note that the data for water depths was missing for nine wells and had a water depth of 0 ft. These values were omitted from the figure.

Figure 3.12 shows the relationship between water depth, TVD, and status code. The water depth and TVD have a negative association. As the water depth increases, the TVD decreases. This trend is opposite of the wells for the entire OCS. Figure 3.12 also shows that the deepest well in this OPD (34,162 ft.) is an outlier. The second deepest well was drilled approximately 10,000 ft. less.

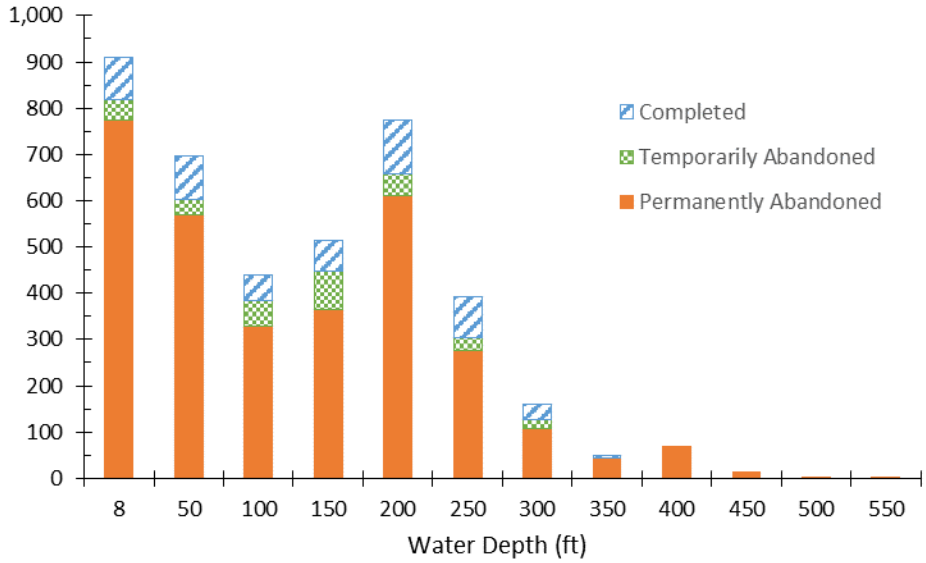

Figure 3.11: Water depth distribution of the wells in the Eugene Island OPD including the distribution of their respective status codes of COM, TA, or PA.

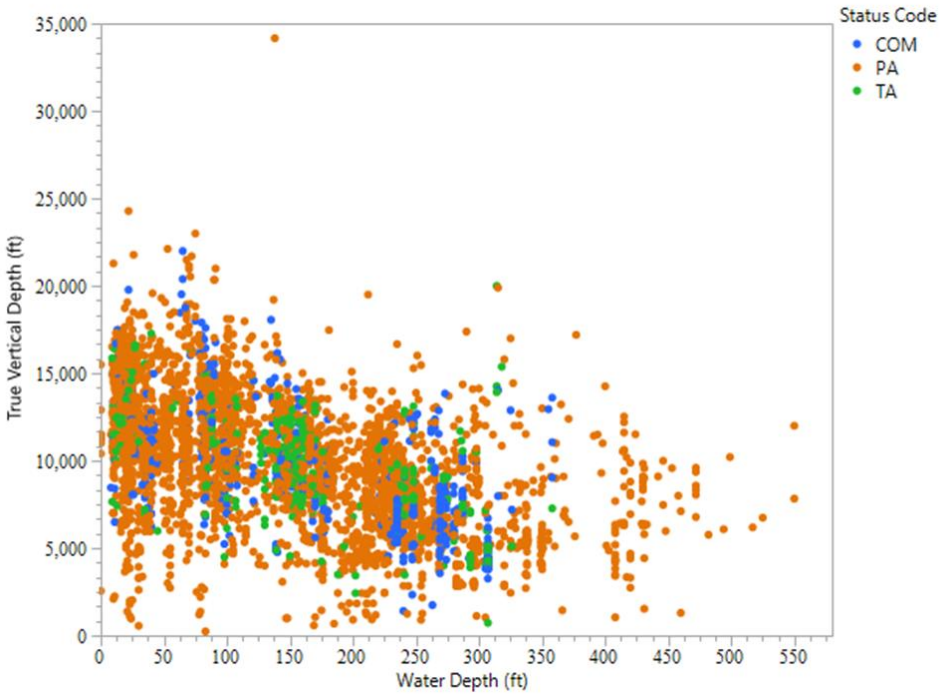

Figure 3.12: Water depth vs. TVD. A negative association between water depth and TVD is shown. The entire OCS had a positive association between water depth and TVD (Figure 3.5).

Figure 3.13 depicts a plot of the spud dates versus the water depth. This plot shows that from the early 1970's, the water depth of the drilled wells started to increase, but all of the deeper wells are PA. The wells that are still producing are in medium to shallow water depths. All of the

TA wells follow the same water depth pattern as the COM wells in that they are in medium to shallow water depths.

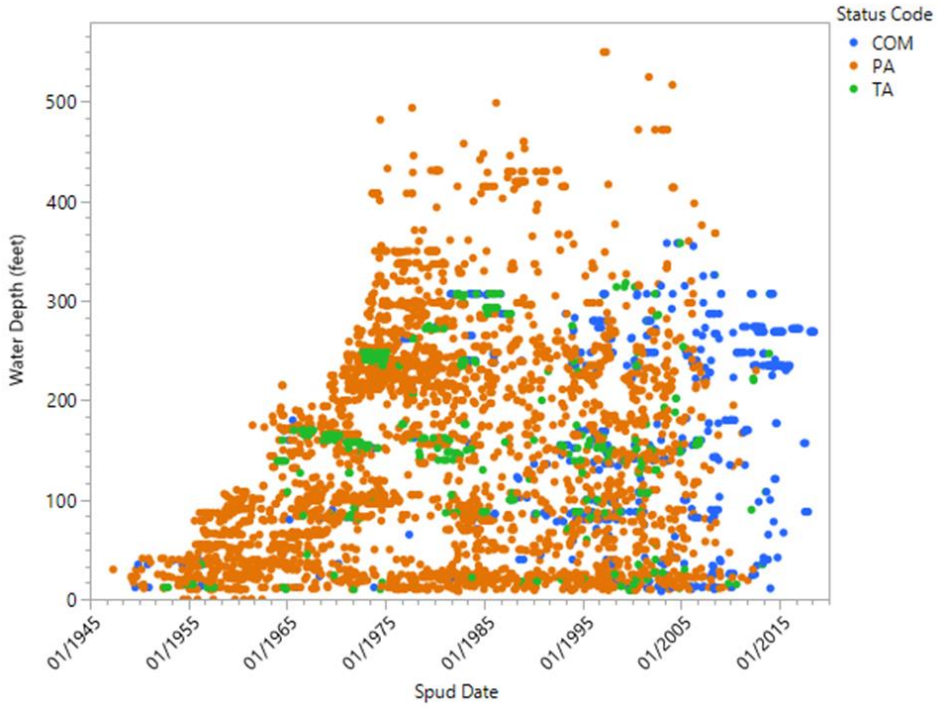

Figure 3.13: Spud date vs. water depth. A positive association between spud date and water depth is shown in this graph similar to Figure 3.4 for all of the wells in the OCS.

Figure 3.14 shows spud date versus total TVD. The total TVD slightly increases as newer wells are drilled, but not drastically (except for the outlier well). Similar to the water depth, the newer wells tend to be in medium to shallow TVD. The majority of the wells drilled from 2010 to the present are still producing.

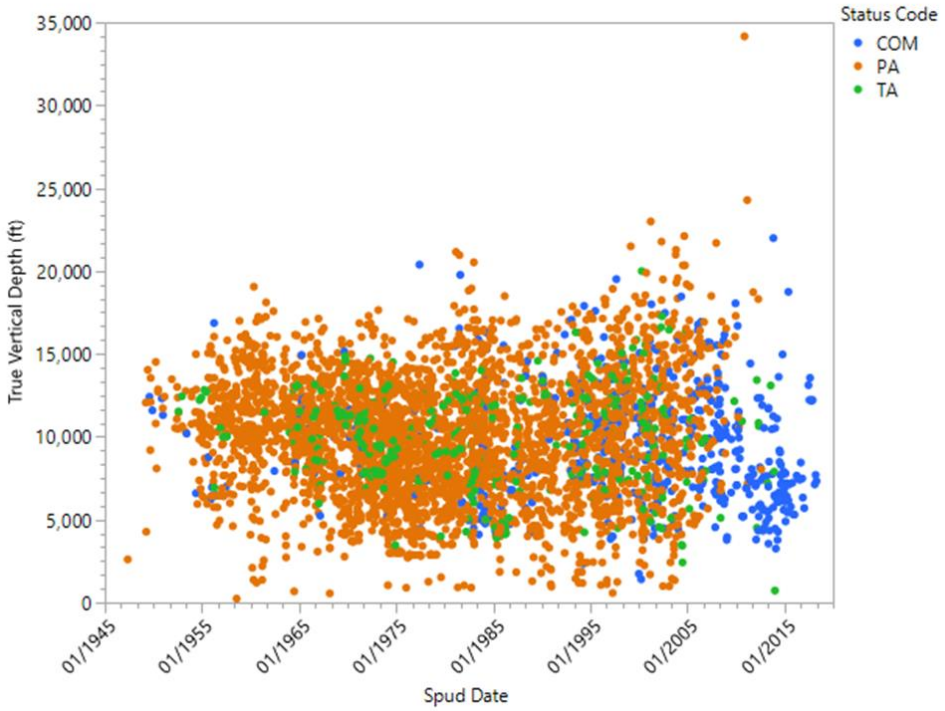

Figure 3.14: Spud date vs. TVD. The majority of the recently drilled wells in the Eugene Island OPD are in medium to shallow water depths, and the majority of these wells are still producing.

After an analysis of all the distribution for wells in the Eugene Island OPD, the typical (i.e. average) well in this region has the following characteristics:

- Status Code: PA
- TVD: 9,808 ± 3604 ft.
- Spud Date: 7/6/1982 ± 15.3 years
- Water Depth: 151 ± 105 ft.

3.2.1. THREE REPRESENTATIVE WELLS

A case study for the Eugene Island OPD will be performed with the characteristics of a medium depth well. The well that was selected as the medium deep well was Well API Number 177100002670. The characteristics of this well are as follows:

Medium Well

- API Well Number: 177100002670
- Status Code: PA
- TVD: 9,889 ft.
- Spud Date: 04/30/1981
- Water Depth: 180 ft.
- Production Data: Yes
- Bottom Hole Pressure (BHP) Gradient: 0.420 psi/ft.

This well is considered as the base well, but we are also interested in the wells on the low and high ends of the TVD, excluding outliers, to create three a representative well scenarios for the OPD. With the two additional cases also analyzed, a total of three case studies will be performed. The criteria for these two extreme wells was TVD, production data, and a BHP that is similar to the medium depth well. The wells on the deep and shallow end of the TVD are as follows:

Deep Well

- API Well Number: 177094046200
- Status Code: COM
- TVD: 19,776 ft.
- Spud Date: 08/07/1981
- Water Depth: 22 ft.
- Production Data: Yes
- BHP Gradient: 0.391 psi/ft.

Shallow Well

- API Well Number: 177104115600
- Status Code: PA
- TVD: 2,614 ft.
- Spud Date: 09/18/1985
- Water Depth: 215 ft.
- Production Data: Yes
- BHP Gradient: 0.490 psi/ft.

The deep and shallow wells do not match all of the desired characteristics (i.e., status code and water depth), but they were selected bases off their total TVD. These two wells will be used to simulate the upper and lower ends of TVD for wells in the Eugene Island OPD. Figure 3.15 depicts a schematic of the three wells: the shallow, the medium, and the deep wells including casing dimensions and depths, casing (or liner) strings, and the approximate locations of the perforations.

The perforations are an important parameter to know because the simulation depth will be set at the bottom of the previous casing strings above the perforations. The reason for this depth is to analyze the barrier above the production horizon to ensure that the cement in the annulus is not damaged and will act as a barrier. The three wells studied are assumed to be vertical wells.

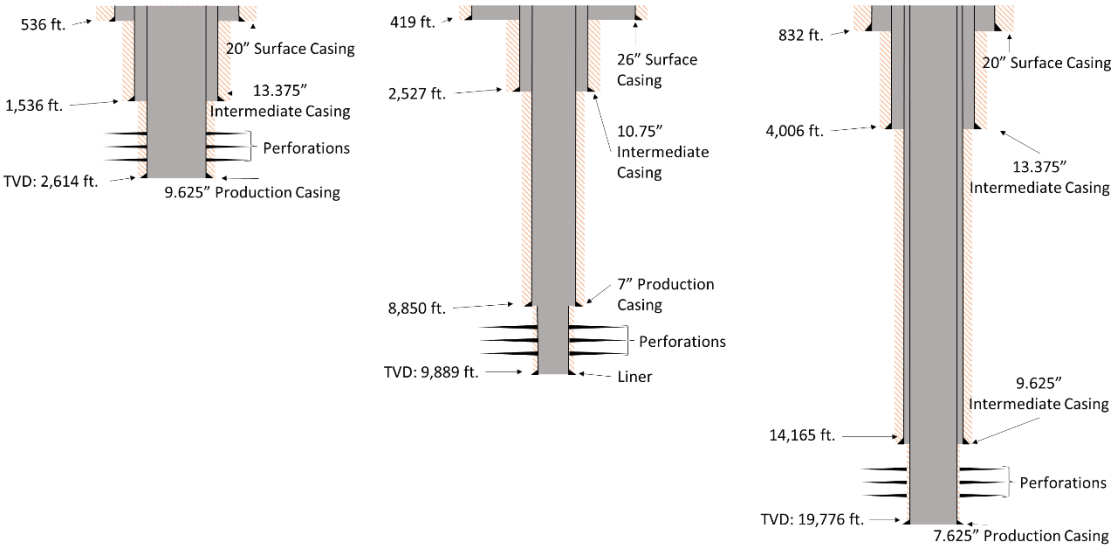

Figure 3.15: Schematic of the shallow well (left), medium well (centered), and deep well (right). Included are the depths of the casing strings, dimensions of the casings, number of casing strings, and the approximate location of the perforations.

3.2.2. OVERBURDEN STRESS

Finkbeiner et al. (1996) performed a study in the Eugene Island OPD in which they determined the overburden stress (σ_v) and minimum horizontal stress (σ_h) for certain depths from available leak-off test (LOT) and fracture completion data. They determined that the minimum horizontal stress had a minimum value of $0.7 * \sigma_v$ to a maximum value equal to σ_v. The range of minimum horizontal stress is shown in Equation 3.1. For a normal stress regime, the maximum horizontal stress (σ_H) has to be between the minimum and overburden stresses. The normal stress regime is showed in Equation 3.2. From Equations 3.1 and 3.2, all three principal stresses can be determined if the overburden stress is known.

$$0.7\sigma_v \leq \sigma_h \leq \sigma_v \tag{3.1}$$

$$\sigma_h \leq \sigma_H \leq \sigma_v \tag{3.2}$$

Finkbeiner et al. (1996) recorded the overburden stress at different depths. The overburden stress can then be converted to gradients by the use of Equation 3.3. Overburden gradients are useful because then the overburden stress can be calculated for any depth.

$$\sigma_{v,gradient} = \frac{\sigma_v}{Depth} \tag{3.3}$$

The problem with the overburden gradients are that they are not constant at different depths; they tend to increase as the depth increases as illustrated in Figure 3.16. A linear and power law approximation can be determined from the gradients such that the overburden gradient can be approximated at a specific depth. The linear approximation used all the overburden stress gradient data while the power law approximation excluded the (4) data points that appear to be outliers. The linear approximation was used to determine the overburden stress for this project since it included all the overburden stress data points. The magnitude difference between the linear and power law approximations for a depth of 8,850 ft. is 2.1%, so the linear approximation was determined to be sufficient. Re-arranging the linear approximation equation results in a solution to determine the overburden stress gradient at a given depth is shown in Equation 3.4.

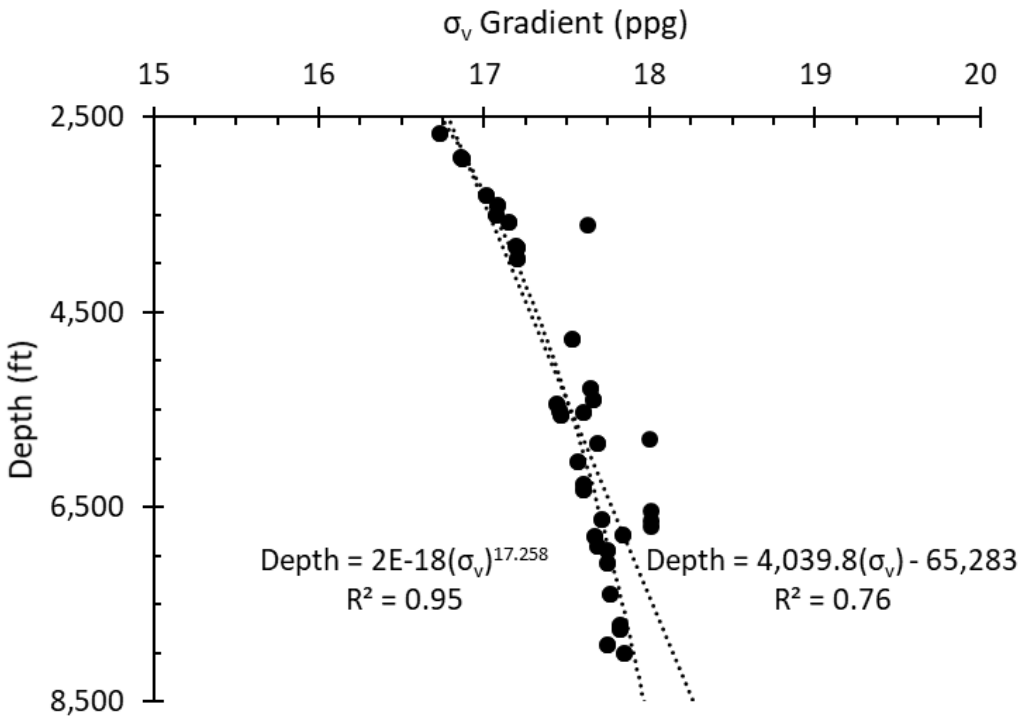

Figure 3.16: Finkbeiner et al. (1996) data converted to overburden stress (σ_v) gradients. A linear approximation was determined such that the overburden gradient can be determined for any depth in the Eugene Island OPD.

$$\sigma_{v,gradient} = \frac{Depth + 65{,}283}{4{,}039.8} \tag{3.4}$$

CHAPTER IV

METHODOLOGY

4.1. FINITE ELEMENT MODELING

The approach used in this study is based off replicating the life cycle of a well from the initial to the later stages as described in Chapter 2.

The FEA model was created and simulated using ANSYS™ 19.1. The model is a 3D poro-elastic model that utilizes a three-dimensional mesh composed of 18,384 CPT216 quadratic brick elements. The element dimensions are designed such that they are smaller towards the center of the model (center of the wellbore) while increasing in size towards the model boundaries. This configuration calculates the stress patterns more accurately in the casing, cement, and near rock formation while saving computational time by having larger elements towards the boundaries. Figure 4.1 shows a 2D and 3D cutaway of the model. Figure 4.1A shows the three different materials included within the model (casing, cement, and rock formation) with their respective finite element grid pattern. Figure 4.1B shows a 3D view of the finite element gridded model.

The large scale dimensions of the model are 1.5 meters in length and width (x, y) and 0.05 meters in height (z). The large scale dimensions are such that the length and width are ten times the ratio of the radius and the boundary (see Chapter 2.2.6 for further explanation). The dimensions of the near wellbore region are based off actual wells from the case study. The near wellbore

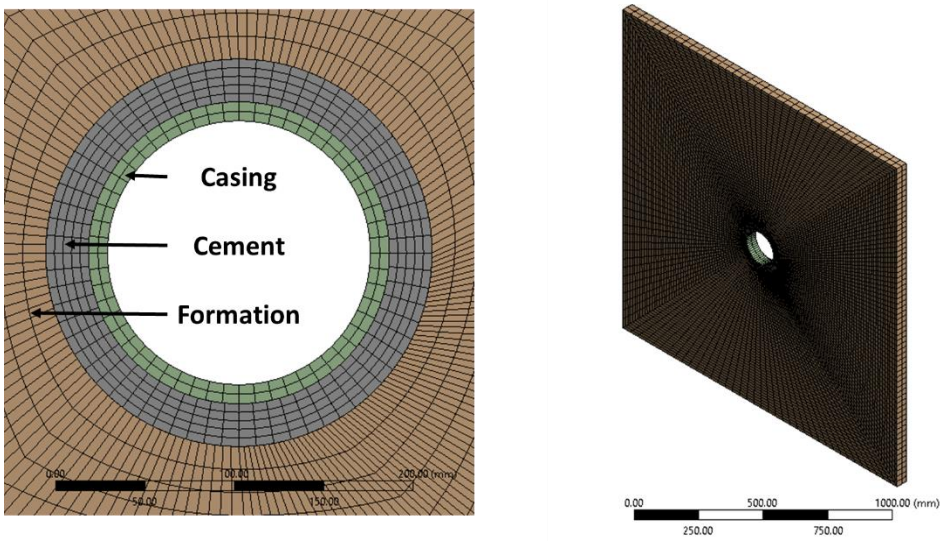

Figure 4.1 A) Cutaway of the well model showing the three different materials included in the near wellbore region with casing (green), cement (gray), and rock formation (brown) and the finite element grid pattern for the materials. B) 3D view of the finite element gridded model consisting of a total of 18,384 elements.

region dimensions change for each case study while the large scale dimensions stay constant for each case study. The model is constrained using frictionless supports on all six sides to represent infinite supports. Along with the ratio of 10 dimensions, the frictionless supports reduce undesired boundary effects. The thickness (height) of the model is 0.05 m thick to represent a 3D cross section of the wellbore.

Figure 4.2 depicts a 3D and 2D (A and B respectively) schematic of the model including the dimensions used in the medium well case study, the far-field stresses, and the internal casing pressure.

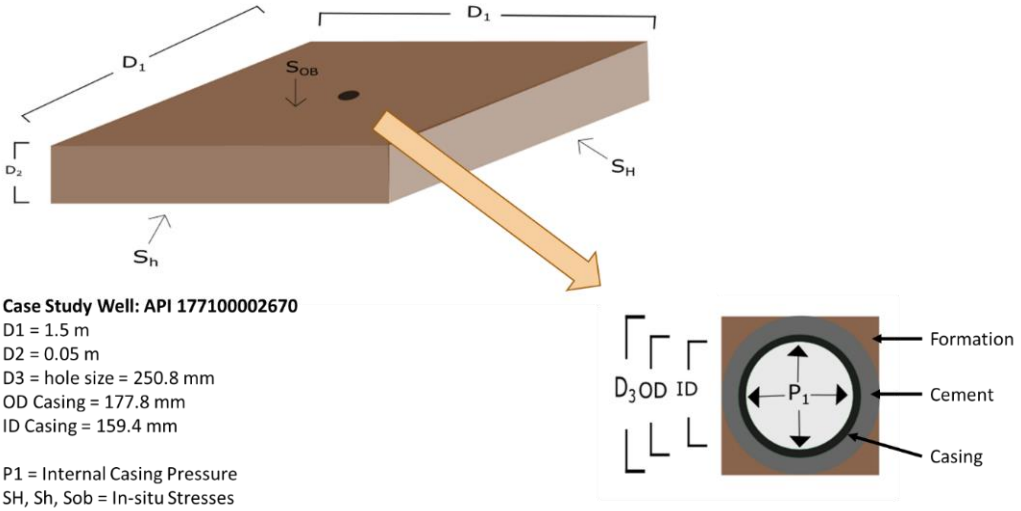

Figure 4.2 A) FEA 3D model schematic with dimensions and far-field stresses for the medium well case study. B) 2D schematic of the medium well wellbore with dimensions and internal casing pressure.

The staged approach uses the property of superposition to build the model's initial conditions before the next load step is implemented. The advantage of performing a staged approach is that the stress and deformation changes can be monitored in each load step. The load steps used within this model were modified from Wiedeman (2014). The load steps are:

Step 1. The model is loaded with horizontal (σ_H & σ_h) and vertical (σ_v) in-situ stresses.

Step 2. The borehole is drilled, and a fluid weight is applied to the rock formation.

Step 3. The casing is added to the borehole with the fluid weight being applied to the inner and outer surfaces of the casing and the borehole.

Step 4. This step represents the completion of the wellbore and has two parts:

a. The cement slurry is pumped into the well. A hydrostatic pressure caused by the cement slurry is applied to the outer surface of the casing and the borehole while the inner casing surface has the fluid weight pressure.
b. Cement hydrates and hardens. The cement elements are added to the model with framework stress, pore pressure, and zero shrinkage assuming the cement is fully bonded to the rock formation and outer casing surface. The hardened cement is inserted with zero deformation but with framework stress in all three principal directions equivalent to the hydrostatic pressure. The fluid weight pressure is still applied to the inner surface of the casing.

Step 5. The wellbore is producing. The fluid weight pressure is removed from the inner surface of the casing and replaced with the production pressure referenced as the "Internal Casing Production Pressure".

The interface between the casing & cement and between the cement & rock formation are assumed to have fully bonded interfaces in this study. The stresses in the casing are calculated assuming it is a linear elastic material since steel does not have a pore pressure. The stresses in the cement and rock formation are calculated assuming poro-elastic materials.

4.2. MODEL PARAMETERS

The input parameters required for the FEA simulations are listed below.

- Depth
- In-situ Stresses
  - σ_v
  - σ_h & σ_H are ratios of σ_v
- Rock Mechanical Properties
  - Young's modulus (E)
  - Poisson's ratio (PR)
- Drilling Parameters
  - Fracture Gradient (P_{frac})
  - Mud Weight (MW)
  - Formation Pore Pressure (Pp)
  - Wellbore Dimensions
- Cement Mechanical Properties
  - Young's modulus (E)
  - Poisson's ratio (PR)
  - Pore Pressure (Pp)
  - Slurry Density
- Production Pressure (BHP gradient)

The input parameters used for the three case studies are listed in Table 4.1 including the source of the values.

Parameter		Well			
		Shallow	Medium	Deep	
TVD	ft.	2,614	9,889	19,776	1
	m	797	3,014	6,028	
Simulation Depth	ft.	1,536	8,850	14,165	*
	m	468	2,697	4,317	
Hole Size	in.	17.50	9.87	12.25	1
	cm	44.45	25.07	31.12	
Casing OD	in.	13.37	7.00	9.63	1
	cm	33.96	17.78	24.46	
Casing ID	in.	12.61	6.28	8.66	1
	cm	32.03	15.95	22.00	
PR Steel		0.30	0.30	0.30	2
E Steel	kpsi	29,008	29,008	29,008	3
	GPa	200.00	200.00	200.00	
Mud Weight	ppg	9.42	11.76	10.76	1
	g/cc	1.13	1.41	1.29	
ICPP	psi	751	3,713	5,545	1
	MPa	5.18	25.60	38.23	
σ_H	psi	1,123	7,178	12,312	4
	MPa	7.74	49.49	84.89	
σ_h	psi	925	5,912	10,140	4
	MPa	6.38	40.76	69.91	
σ_v	psi	1,321	8,446	14,486	4
	MPa	9.11	58.23	99.88	
Pp Rock	ppg	8.26	11.26	9.84	1
	g/cc	0.99	1.35	1.18	
PR Rock		0.27	0.27	0.27	3
E Rock	kpsi	3,626	3,626	3,626	2
	GPa	25.00	25.00	25.00	
Pp Cement	ppg	8.26	11.26	9.84	*
	g/cc	0.99	1.35	1.18	
PR Cement		0.25	0.25	0.25	2
E Cement	kpsi	1,450	1,450	1,450	2
	GPa	10.00	10.00	10.00	
Cement Slurry	ppg	10.17	12.76	12.92	1
	g/cc	1.22	1.53	1.55	
Cement Stress	psi	815	5,845	9,516	*
	MPa	5.62	40.43	65.61	
Cement UCS	psi	5,802	5,802	5,802	3
	MPa	40.00	40.00	40.00	
Cement Tensile Strength	psi	435	435	435	3
	MPa	3.00	3.00	3.00	
Cement Cohesion	psi	2,176	2,176	2,176	3
	MPa	15.00	15.00	15.00	
Cement Friction Angle	°	30.00	30.00	30.00	3

[1]Log, [2]Zhang et al. (2016), [3]Weideman (2014), [4]Finkbeiner et al. (1996)

Table 4.1: Base case parameters for the three wells in the Eugene Island OPD and the source of their values. ICCP is internal casing production pressure.

The simulation depth was chosen to be the depth of the deepest casing string before the production zones in the well. The cement sheath can be assumed to be intact and not damaged from perforations at this location. The TVD of the well would not be relevant for modeling cement sheath integrity since it is below the perforation and production zones and not acting as a barrier in preventing hydrocarbon migration or fresh water contamination. The cement sheath located at and/or above the perforations either is damaged or has a potential to be damaged from the perforation procedure. The extent of the damage is not known and was not investigated in this study. The cement sheath at shallower depths of the wells was not investigated either. The sheaths at shallow depths can include multiple casings and (potentially) multiple cement sheaths. The additional parameters would complicate the model and the contributing stress development factors could be altered. Therefore, the single cement sheath and single casing was investigated to determine which parameters cause the stress development for a single casing, cement sheath, and rock formation that is the primary barrier in preventing leakage or water contamination above the production zone (perforations).

The in-situ stress gradients for the Eugene Island OPD was based on Finkbeiner et al. (1996) as discussed in Chapter 3.2.2. Values of shale mechanical properties were used for the rock formation based off Zhang et al. (2016) and Weideman (2014).

4.2.1. WELLBORE PROPERTIES

When the well is drilled, the fracture gradient, pore pressure, and drilling fluid density are determined and used to drill the well safely and efficiently. This data is usually found in the well completion reports, yet the medium well did not contain all of this data explicitly in the well completion reports. Therefore, offset well completion reports were used to predict the formation properties.

Wells drilled after 2004 have all of their completion reports available online in the BSEE database. The formation fracture gradient, formation pore pressure, and mud weight used to drill the well are available in the completion reports. The medium well (API Number: 177100002670) is located in Block 276 of the Eugene Island OPD, and all of the (post-2004) well completion reports of wells drilled in Block 276 of Eugene Island were examined. Formation pore pressure, formation fracture gradient, and mud weight for the offset wells are shown in Figure 4.3.

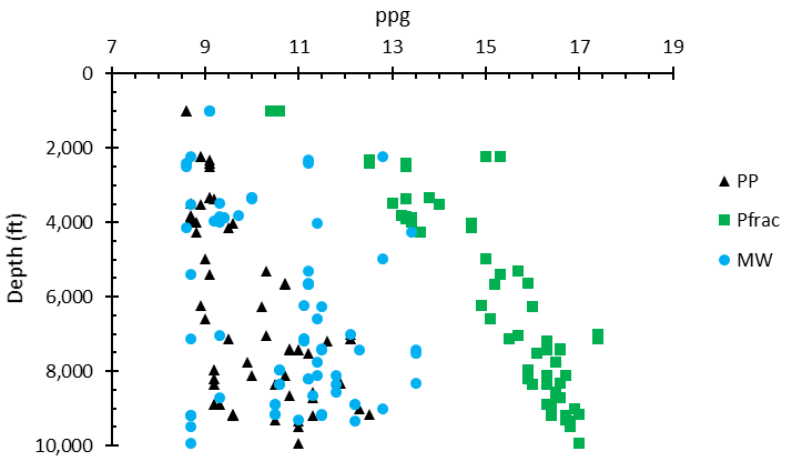

Figure 4.3: Eugene Island Block 276 well completion report values of 79 wells used for offset well data for the medium well case study.

The mud weight data could be used to determine the cement slurry density by assuming the cement slurry density is equal to the mud weight density. This may be a valid assumption, but the well completion reports provide the amount of cement used while casing the well. This data can be used with the wellbore dimensions to determine the cement slurry density.

4.2.2. CEMENT MECHANICAL PROPERTIES

The cement slurry density has already been determined from the well logs. The cement setting stress is assumed to be equal to the hydrostatic column of the cement slurry. The cement sheath in assumed to have a porosity with a finite permeability which allows the pore pressure in the surrounding rock formation to infiltrate the cement pores resulting in the cement having a pore

pressure equal to the surrounding rock pore pressure. The mechanical properties of the cement are determined from values used by Zhang et al. (2016).

4.2.3. PRODUCTION PRESSURE

Initial reservoir pressure was based on static BHP measurements. The production pressure is assumed to be the internal casing pressure at the production step of the simulations.

4.3. PARAMETRIC ANALYSIS

The parametric variation for all of the parameters, unless otherwise stated in Table 4.2, are ± 40% of the base case values to see how variation in properties can alter the stress development in the cement sheath.

Parameter	Low	High
Cement Stress (MPa)	MW	P_{Frac}
Pp Cement (g/cc)	0	Rock Pp
Isotropic Horizontal Stress Variation	$\sigma_v = \sigma_{v,\,base}$ $\sigma_H = 0.7 \times \sigma_{v,\,base}$ $\sigma_H = \sigma_{h,\,base}$	$\sigma_v = \sigma_{v,\,base}$ $\sigma_H = 1 \times \sigma_{v,\,base}$ $\sigma_H = \sigma_{h,\,base}$
Anisotropic Stress Variation	$\sigma_v = \sigma_{v,\,base}$ $\sigma_H = 0.7 \times \sigma_{v,\,base}$ $\sigma_h = 0.7 \times \sigma_{H,\,base}$	$\sigma_v = \sigma_{v,\,base}$ $\sigma_H = 1 \times \sigma_{v,\,base}$ $\sigma_h = 0.7 \times \sigma_{H,\,base}$
Vertical Stress Variation	$\sigma_v = -5\% \times \sigma_{v,\,base}$ $\sigma_H = \sigma_{h,\,base}$ $\sigma_h = 0.7 \times \sigma_{v,\,base}$	$\sigma_v = +5\% \times \sigma_{v,\,base}$ $\sigma_H = \sigma_{h,\,base}$ $\sigma_h = 0.7 \times \sigma_{v,\,base}$

Table 4.2: High and low values for the parametric study. These values apply for all three well depth parameters.

The cement stress boundaries are a maximum stress equal to the fracture pressure of the rock formation and a minimum stress equal to the mud weight (MW). Any stress values above or below those will result in instability of the borehole during well construction. The cement P_p can

either have a minimum value of zero or a maximum P_p equal to the surrounding rock formation (base case). The in-situ stresses were changed so that the horizontal stresses vary from a combination of isotropic to anisotropic stresses and the vertical stress is off by ± 5%. All of these scenarios are displayed in Table 4.2 for the high and low envelopes for the parametric analysis.

4.4. STRESS DATA COLLECTION

The stress points chosen for the data analysis are along the x-axis at the casing/cement and cement/rock formation interfaces. The stresses (hoop and radial) will be measured in the cement along the casing/cement and cement/rock formation interfaces to monitor for potential debonding. The locations of the stress measurement points are illustrated in Figure 4.4. The stress results from the interfaces will be referred to as quantitative results.

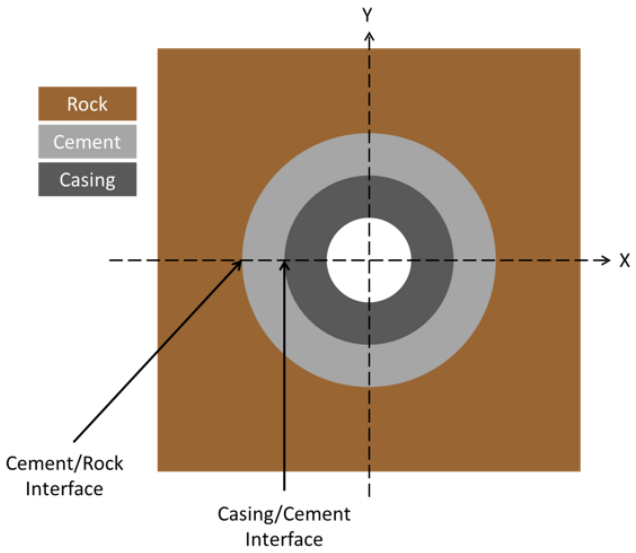

Figure 4.4: Quantitative measurement points along the x-axis where the effective cement stress is monitored for potential debonding.

CHAPTER V

RESULTS

The results for this project are presented in four sections. Section 5.1 contains the results of comparing a staged FEM versus a not staged FEM. The analytical solution for stress along a radius for the wellbore compared to the stress determined by the FEM is discussed in Section 5.2. Section 5.3 presents the results for the base wellbores, and Section 5.4 contains the parametric analysis for the three wells.

5.1. STAGED FEM

Modeling the well cycle requires a staged finite element approach which allows the stress and deformations to be monitored in each loading step. Figure 5.1 shows two model wellbores with each depicting the hoop and radial stress throughout the cement sheath. The model on top is a staged model following the load steps described previously while the lower model is not staged and has the far field stresses, cement framework stress, and internal casing pressure applied in a single time step. Figure 5.1 shows that when all the load steps and initial conditions are put in a single step, the resulting stress patterns do not accurately depict the stresses at the interfaces for the radial stress. The cement/rock formation interface's radial stresses are not constant throughout the cement and do not match between the interfaces of the casing/cement and the cement/rock formation. The cement sheath along the cement/rock formation interface violates Newton's Third Law as marked on Figure 5.1. No external force is applied to the cement or casing, therefore, the radial stress should be equal throughout the cement sheath along both interfaces (Weideman, 2014).

Instead, the effective radial stress is less in the marked section of the cement sheath along the casing/cement interface than the cement along the cement/rock interface. The hoop stress in the cement sheath shows a similar pattern for the non-staged model. The hoop stress changes in the cement sheath when it should be constant throughout.

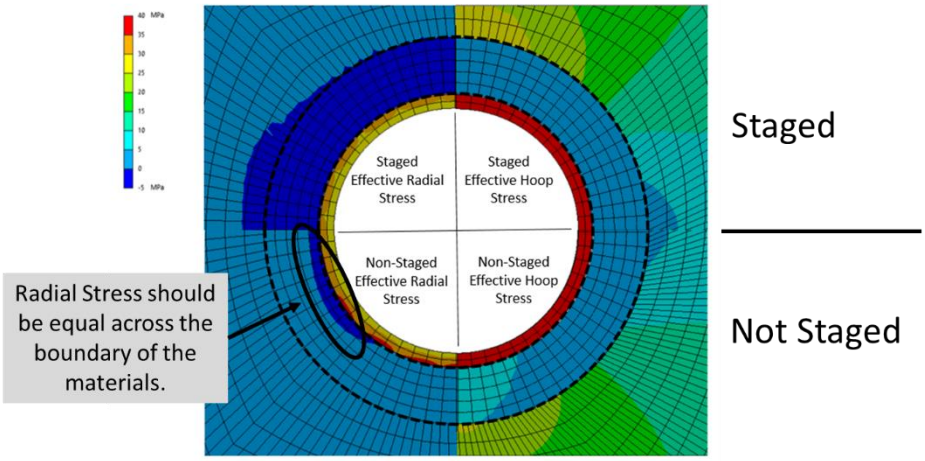

Figure 5.1: Staged FEM (top) compared to non-staged FEM (bottom).

5.2. ANALYTICAL VALIDATION

The numerical wellbore integrity model was verified using of the analytical equations given in Chapter 2.4.1. The results for the model are shown in Figure 5.2 along with the results for the analytical solution. The poro-elastic FEA model has a 3% maximum variation from the analytical solution indicating that the model is an accurate representation of stress development for the casing, cement, and rock formation of a wellbore. Given the accuracy of the numerical model compared to the analytical solution, the parameters can be modified with parameters from the case studies to represent the shallow, medium, and deep wells, and the results can be used to determine if the cement sheath is experiencing failure.

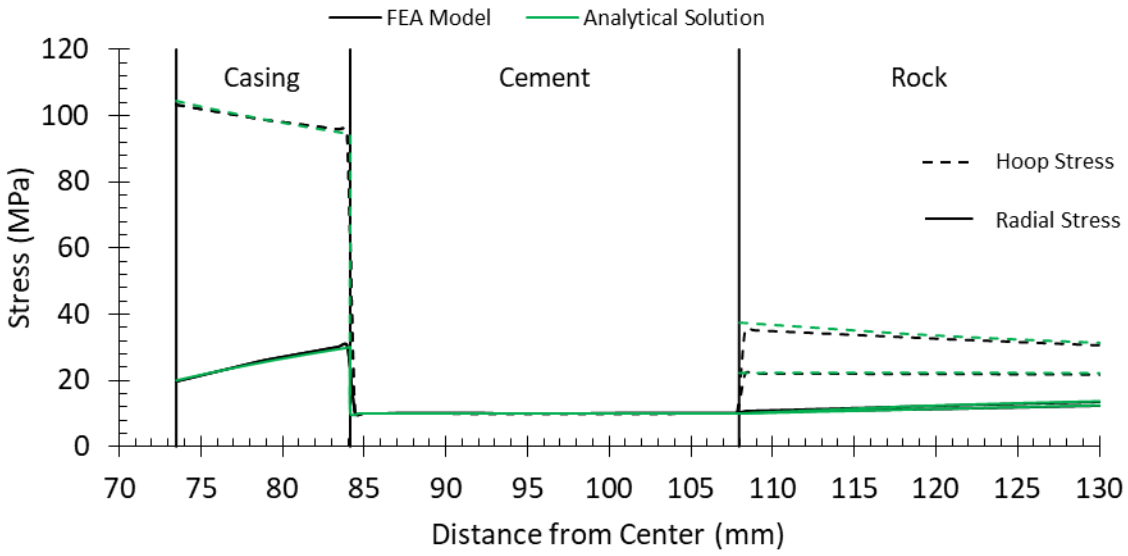

Figure 5.2: FEA analysis compared to the analytical solution showing less than 3% variation.

5.3. BASE CASE WELLBORES

For the first part of the results analysis regarding potential cement sheath debonding and cement fracturing, three base case wellbores were simulated. The effective stresses (hoop and radial) of the cement sheath is presented for the casing/cement and cement/rock formation interfaces.

The effective stress results for the base case parameters of the three wells are represented in Table 5.1. The medium depth well results are considered the standard and the shallow and deep depths are normalized to the medium well. The shadowed coloring indicates tensile stresses while the others are compressive. The base results show that the medium and deep wells are experiencing tensile stresses in the radial directions which indicate debonding as defined in Chapter 2.3.2. The medium depth well is debonding at both the casing/cement and cement/rock interfaces while the deep well is only debonding at the casing/cement interface. The shallow depth well is not experiencing any tensile stresses, but it should be noted that the effective stresses are close to the

tensile range. Disking of the cement sheath is not a concern for the three wells since the effective vertical stresses are all compressive.

Effective Interface Stresses	Well		
	Shallow	Medium	Deep
		MPa	
Hoop Stress Casing/Cement	-84%	5.70	167%
Hoop Stress Cement/Rock	-78%	3.70	242%
Radial Stress Casing/Cement	-121%	-2.75	-59%
Radial Stress Cement/Rock	-174%	-0.84	-390%
Vertical Stress Casing/Cement	-70%	3.03	276%
Vertical Stress Cement/Rock	-71%	3.01	287%

Compressive	Tensile

Table 5.1: Cement sheath effective stress results for the base case parameters for the three case studies. The shallow and deep well are normalized to the medium well.

To analyze the potential of shear failure, a Mohr-Coulomb graph was used to evaluate whether the shear stresses were in failure as shown in Figure 5.3. Figure 5.3 shows that all three wells are far from being in shear failure. The deepest well proves closest to shear failure, but the gap between its Mohr circle and the failure envelope is significant. An interesting observation is that the shear stresses in the shallow well are not significant. The stresses are barely visible when compared to the medium and deep wells let alone the failure envelope. Another observation is that Figure 5.3 shows that the medium well has tensile stresses at both interfaces and the deep well has tensile stresses at the casing/cement interface as shown by their respective Mohr circles crossing the tensile cutoff.

Figure 5.4 depicts the graphical results of the base case cement sheaths for the three wells. The effective radial stresses are depicted on the left, and the effective hoop stresses are shown on the right. The inner radius of the sheath is the casing/cement interface while the outer radius is the cement/rock formation interface.

For the shallow well, the maximum effective stress is 1 MPa and is not experiencing any tensile stresses. The medium well is experiencing tensile radial stress throughout the cement

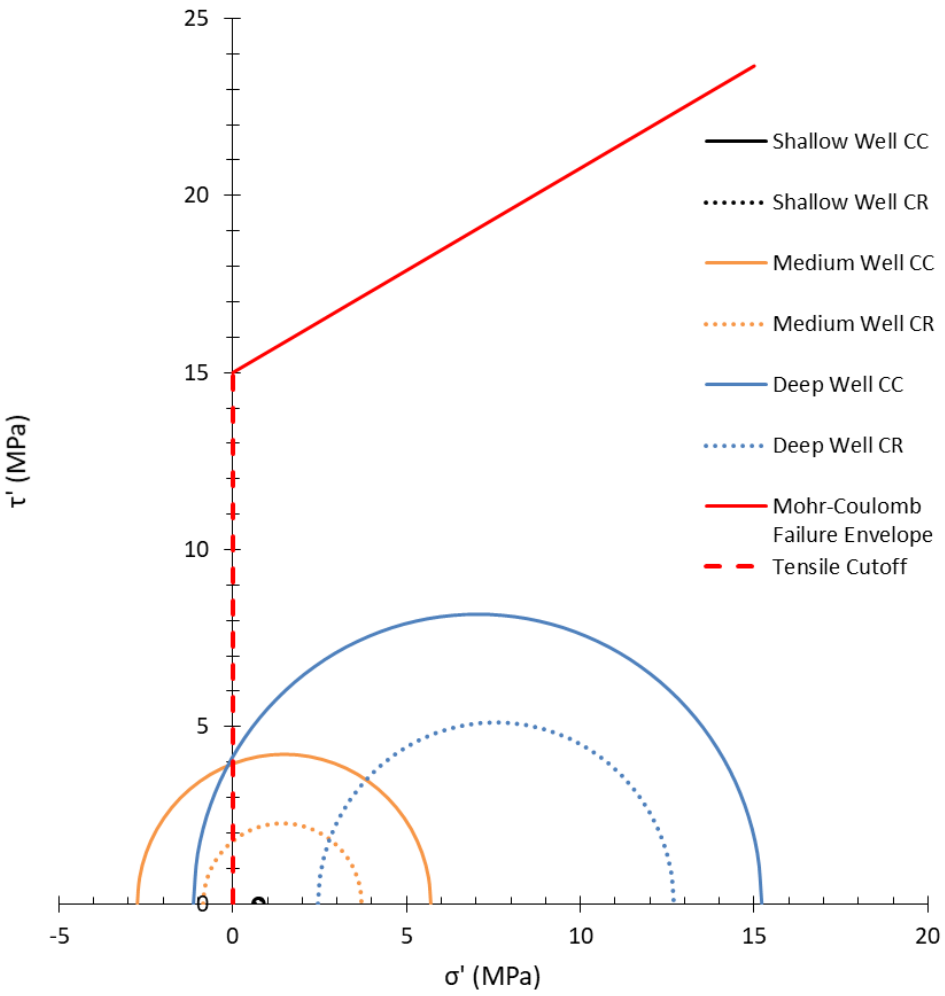

Figure 5.3: Shear failure envelope of cement compared to the cement sheath for the three base case wells.

sheath, and the magnitude is higher along the casing/cement interface implying that the resulting debonding gap would be greater than along the cement/rock interface. The deep well is only experiencing debonding along the casing/cement interface as indicated in Table 5.1 and Figure 5.4. It is important to note that the effective hoop stresses have variances due to the anisotropic in-situ stresses but is masked in Figure 5.4 due to the scale resolution. The effective hoop stresses for the medium and deep wells are not close to the tensile range, (therefore not resulting in radial cracks) and consequently not of interest to this discussion.

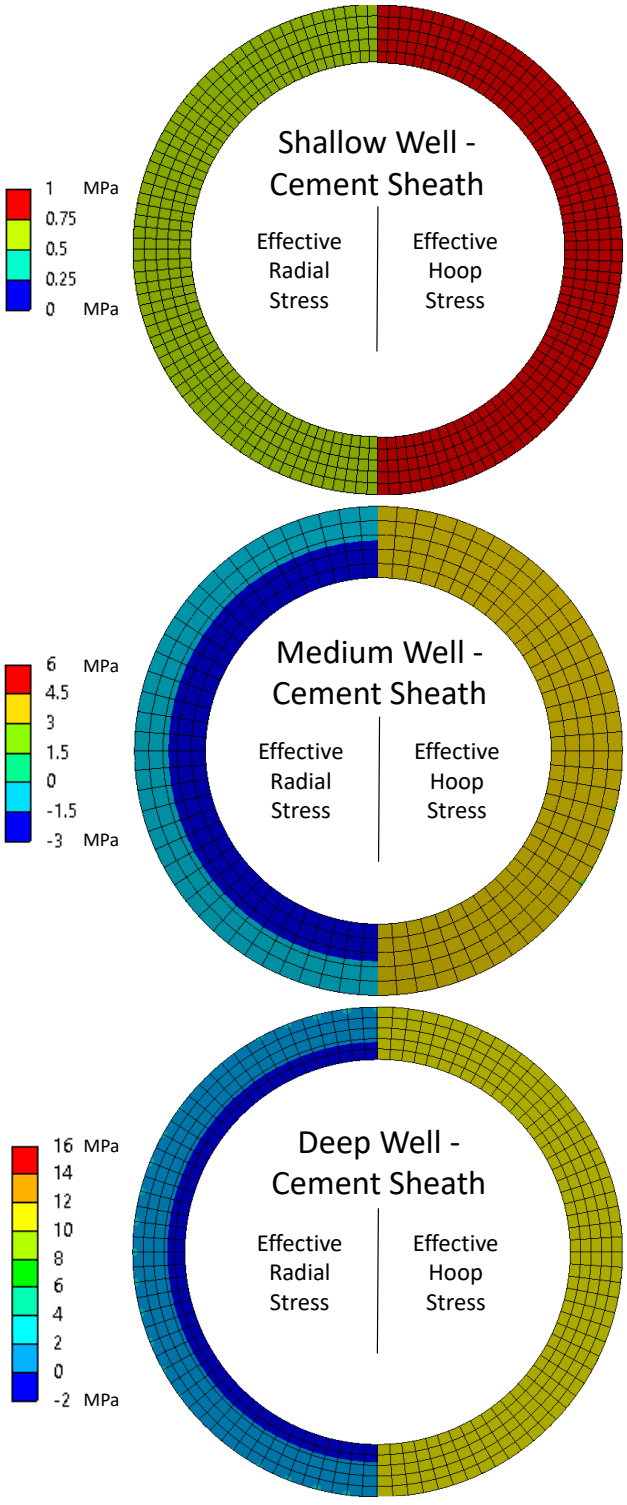

Figure 5.4: Graphical results of the base case stress values shown in Table 5.1 for the three case studies; shallow, medium, and deep wells.

The results of the medium and deep well base case simulations are in agreement with an analysis from the literature. These two wells experienced debonding after the production step when the mud weight pressure inside the casing changed to a production pressure. Previous studies have documented that changes in thermal cycling can cause cement sheath debonding (Lavrov et al., 2015; Zhang et al., 2017) while Nygaard et al. (2014) concluded that debonding at the casing/cement interface occurs as a result of thermal and pressure changes. It should be noted that Zhang et al. (2017) observed debonding as a result of thermal cycling of cooling fluid at the cement/rock interface whereas the results shown here conclude that debonding is occurring at the casing/cement interface.

5.4. PARAMETRIC ANALYSIS

The second part of this study is the parametric study of the base case wells to rank the stress contributing factors. The raw data for the parametric analysis is listed in Table A.1 in Appendix A. The interpretation of the results are shown in Figure 5.5, Figure 5.6, and Figure 5.7 for the shallow, medium, and deep well respectively. The maximum and minimum normalized effective stress values from the three wells are shown. The parameters are ranked from largest to smallest percent change with respect to the effective radial stress at the cement/rock formation interface. Due to the large variation of the parameters, log scales were used for the x-axis. The solid bars represent a positive percent change while the checkered bars represent a negative percent change.

Figure 5.5, Figure 5.6, and Figure 5.7 show that the ranking of the parameters are not the same for all three wells. All three wells have cement Pp listed as the most important contributing factor, but the ranking of the parameters after that change. The medium and deep well are the most similar; both have the same order of parameters until the in-situ stresses. For the shallow well, the setting stress of the cement is more critical than the internal casing pressure, and the

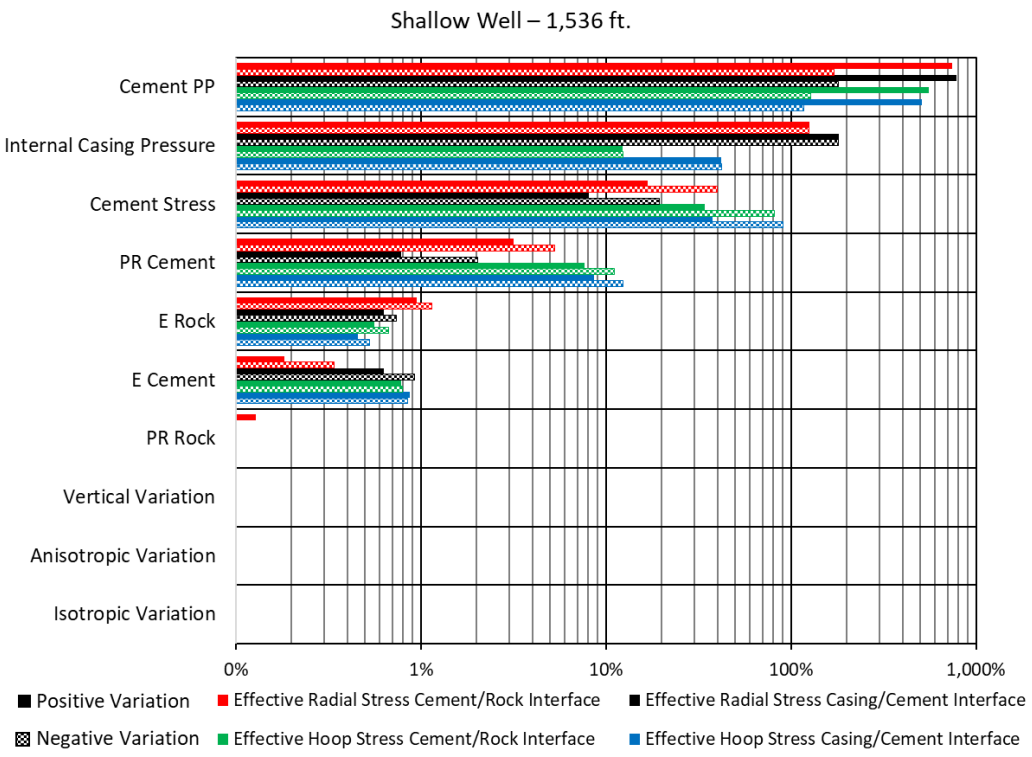

Figure 5.5: Results of the parametric study ranking the parameters with the largest impact on stress development for the shallow well in the Eugene Island OPD.

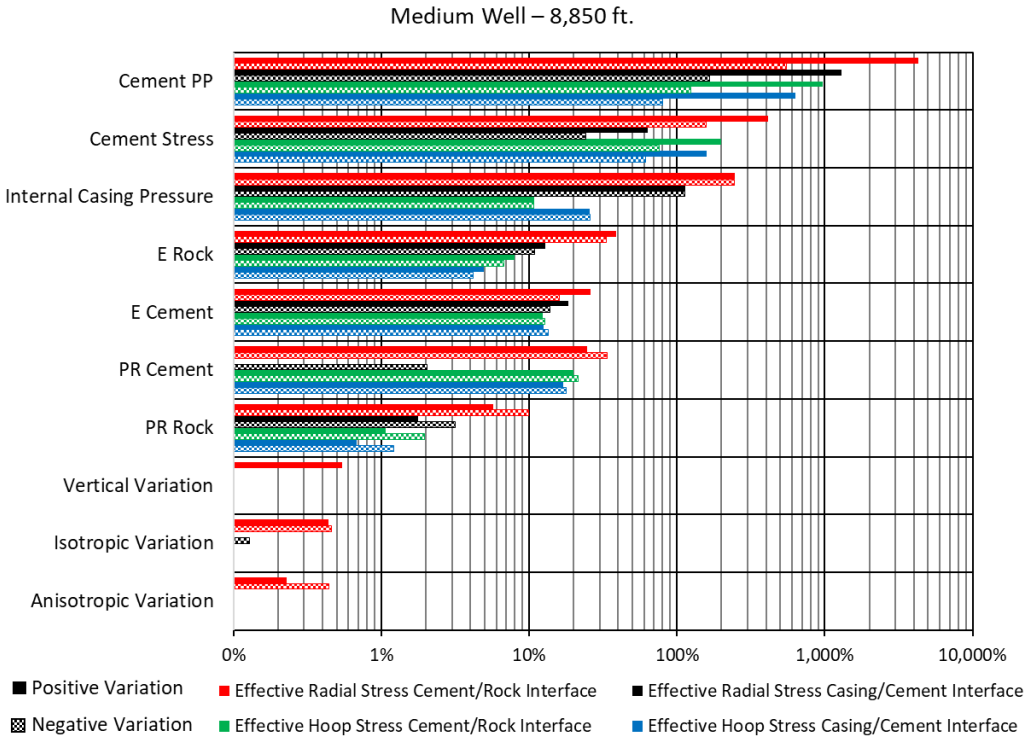

Figure 5.6: Results of the parametric study ranking the parameters with the largest impact on stress development for the medium well in the Eugene Island OPD.

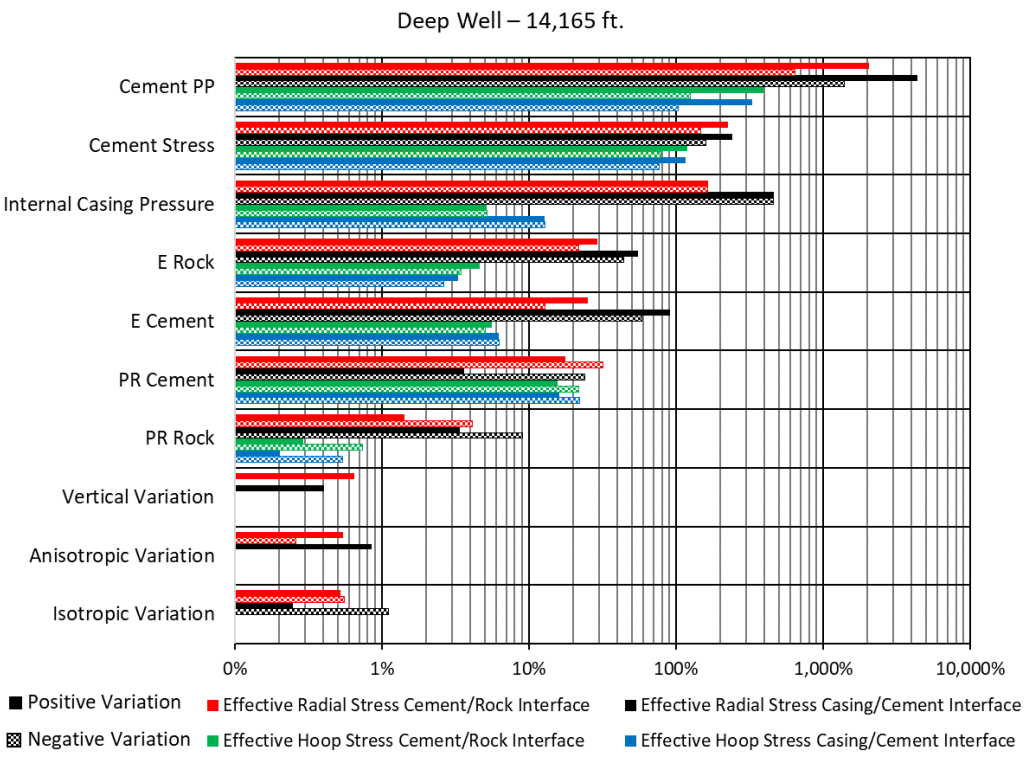

Figure 5.7: Results of the parametric study ranking the parameters with the largest impact on stress development for the deep well in the Eugene Island OPD.

mechanical properties of the surrounding rock formation and cement are different from the other two wells. Overall, the general interpretation of the three figures (Figure 5.5, Figure 5.6, and Figure 5.7) are similar for all three wells: the cement hydration parameters and the internal casing pressure are the most critical parameters in the stress development of the cement sheath, followed by the mechanical properties of the rock and cement, and lastly, the in-situ stresses have little impact on the stress development in the sheath. Another observation is that the radial stresses are more sensitive to parameter changes than the hoop stresses which indicates that variation of parameters are more likely to lead to tensile debonding than radial cracks.

The results of this study are in agreement with Bois et al. (2011) in which the authors state that the two most critical aspects of cement sheath integrity are the cement hydration parameters and changes in pressure in the wellbore. The changes in internal casing pressure have already been proven in the literature to be a major cause of cement sheath debonding and will not be discussed

further, yet the cement hydration parameters (setting stress and pore pressure development) have not been studied as intensely. Simulating the setting stress from the maximum possible value (P_{Frac}) to the lowest possible scenario (zero effective stress) significantly affects the cement sheath stress by 100% in both the radial and hoop stresses. The change in effective stresses is significant enough to take the cement sheath from compressive to tensile and vice versa. The cement P_P acts the same way. A maximum P_P (equal to the setting stress resulting in an effective stress of zero) and a minimum P_P (zero P_P) affects the cement stress from 100% to greater than 1,000% in some instances. Both of these parameters are critical in the development of the hydration of cement, but they are not well understood. The upper and lower ranges for both parameters presented in this paper are realistic, but the variation has dramatic results. Therefore, cement hydration should be investigated further to develop a better understanding of how the cement setting stress and P_P develop during cement hydration.

When designing a cementing job to complete a well, many factors go into it. The cement density is arguably the most critical factor, but the structural properties of hardened cement should also be considered. The only changeable parameters for the cement job are the cement composition which directly affects the mechanical properties, such as E, PR, UCS, and bonding strength. From the results of this study, the mechanical parameters have less effect on cement sheath integrity. The effective radial and hoop stresses were less sensitive to changes in the mechanical properties of cement. The maximum change in one of said parameters is approximately 20% (except for a few instances with the deep well) which will not change of any of the baseline effective stresses results in Table 5.1 from being in compressive to tensile or vice versa. Therefore, changing cement compositions to develop enhanced structural properties is not dominant in cement sheath integrity in terms of radial cracks, disking, or tensile debonding. This result is not in agreement with Fleckenstein et al. (2001) in which they concluded that ductile cements (high PR & low E) would "significantly" reduce tangential (hoop) tensile stresses, but the authors did not take into account

pore pressure of the cement. The results of this paper do appear to agree with Nygaard et al. (2014) in which the mechanical properties of the intact cement do not affect the radial stresses dramatically.

Another trend seen for all three wells is that changing the in-situ stresses have less than 1% effect on the stress development in the cement sheath. This indicates that the geologic location of the well has little impact regarding the potential failure of the cement sheath in vertical wells for normal faulting stress regimes although the changes of in-situ stresses due to compaction and subsidence, which was not addressed in this study, have been shown to play a factor in casing shear as described by Dusseault et al. (2001).

A final result, that is not as obvious and is not explicitly shown from the parametric study, is how the depth of the well affects cement sheath stress. The shallow well is not experiencing debonding at either interface, but both the medium and deep wells are experiencing at least one interface debonding. The medium well is experiencing debonding at both interfaces while the deep well is only debonding at one interface implying that there is a depth in which the cement sheath will be at a higher risk to develop gaps. This depth versus risk of debonding curve may look similar to a bell curve as seen with the three wells presented in this paper. There may be an "optimum" depth that puts wells at a higher risk for debonding, but above and below that depth have less prime conditions. This reasoning would explain why the medium depth well appears to be debonding at both interfaces, but the deep well is only debonding at one interface. This phenomenon was described by Gray et al. (2009) in which they concluded that debonding does not always occur at the deepest locations within a wellbore.

CHAPTER VI

CONCLUSION

6.1. SUMMARY

A staged 3D finite element wellbore integrity model based off actual wellbore dimensions for three wells in the Eugene Island OPD has been developed, and a parametric study has been performed to rank contributing factors of stress development that lead to potential cement sheath debonding.

The main conclusions of this study are as follows:

- The base case parameters for the medium and deep TVD wells experience debonding on at least one interface between the casing and cement and/or the cement and rock formation leading to concerns that established wells in the GoM are experiencing leakage.
- Tensile debonding is the most probable form of cement sheath failure for vertical wells in the Eugene Island OPD.
- The depth of the well appears to be a contributing factor in causing cement sheath debonding. The results of this study show that specific depths are more prone to cause debonding than others.

- Cement hydration properties (setting stress and P_P) and the internal casing pressure have the most significant effect on the stress development in the cement sheath. The literature shows that the internal casing pressure is critical in cement sheath debonding, but the cement hydration parameters have not been well documented. These two parameters have major assumptions associated with them and need to be studied further to know definitively how they affect cement sheath stress.

- Cement mechanical properties, E and PR, have little effect on cement sheath stress development, and the variations are not large enough to sway the cement stress into or out of failure.

- The geographic location of the well has little to no effect on the potential for cement sheath debonding in vertical wells.

6.2. FUTURE WORK

The results of this thesis indicate that debonding of the cement sheath to the casing and/or rock formation are the predominate forms of cement sheath failure. However, the gaps created due to debonding were not determined in this study. Future work should include quantifying gap widths between the cement sheath and the interfaces to determine if hydrocarbon migration is possible along with determining if the debonding that is occurring is propagating to the surface resulting in hydrocarbon leakage.

REFERENCES

Anderson, E. M. 1951. *The dynamics of faulting and dyke formation with applications to Britain*. Second Edition, Edinburgh: Oliver and Boyd. 206.

Bensted, J. and Barnes, P. 2002. *Structure and Performance of Cements*: CRC Press. 565.

Bois, Axel-Pierre, Garnier, Andre, Rodot, Francois et al. 2011. How to Prevent Loss of Zonal Isolation Through a Comprehensive Analysis of Microannulus Formation. *SPE Drilling & Completion* 26 (01): 13-31. https://doi.org/10.2118/124719-PA.

Bois, A. P., Garnier, A., Galdiolo, G. et al. 2012. Use of A Mechanistic Model to Forecast Cement-Sheath Integrity. *SPE Drilling & Completion*, *27*(02), 303-314. https://doi.org/10.2118/139668-PA.

Bosma, M., Ravi, K., van Driel, W., and Schreppers, G.J. 1999. Design Approach to Sealant Selection for the Life of the Well. Paper SPE 56536 presented at the SPE Annual Technical Conference and Exhibition, Houston, 3–6 October. doi: 10.2118/56536-MS.

Bradley, W. B. 1979. Failure of inclined boreholes. *Journal of Energy Resources Technology*, *101*(4), 232-239.

Cooke, C. E., Jr., Kluck, M. P., and Medrano, R. 1983. Field Measurements of Annular Pressure and Temperature During Primary Cementing. *Journal of Petroleum Technology* 35 (08): 1429-1438. https://doi.org/10.2118/11206-PA.

Data.bsee.gov. 2018. *Borehole Online Query*. [online] Available at: https://www.data.bsee.gov/Well/Borehole/Default.aspx [Accessed 13 Sept. 2018].

Dusseault, M. B., Bruno, M. S., & Barrera, J. (2001, June 1). Casing Shear: Causes, Cases, Cures. Society of Petroleum Engineers. doi:10.2118/72060-PA

Finkbeiner, T., Stump, B. B., Zoback, M. D. et al. 1996. Pressure (Pp), overburden (Sv), and minimum horizontal stress (SHMIN) in Eugene Island Block 330, offshore Gulf of Mexico. Topical report, April 1-July 1, 1996(No. PB-97-124549/XAB). Pennsylvania State Univ., University Park, PA (United States). Dept. of Geosciences.

Fjaer, E., Holt, R. M., Horsrud, A .M., Raeen, A. M., and Risnes, R., 2008. *Petroleum Related Rock Mechanics*. Second edition, Elsevier publishing. 491.

Fleckenstein, W.W., Eustes, A.W. III, and Miller, M.G. 2001. Burst-Induced Stresses in Cemented Wellbores. SPE Drill & Compl 16 (2): 74–82. SPE-72059-PA. doi: 10.2118/72059-PA.

Gray, K. E., Podnos, E., & Becker, E. 2009. Finite-Element Studies Of Near-Wellbore Region During Cementing Operations: Part I. *SPE drilling & completion* 24(01), 127-136. https://doi.org/10.2118/106998-PA.

Hiramatsu, Y., & Oka, Y. 1968. Determination of the stress in rock unaffected by boreholes or drifts, from measured strains or deformations. *International Journal of Rock Mechanics and Mining Sciences & Geomechanics Abstracts* (Vol. 5, No. 4, pp. 337-353). Pergamon.

Jaeger, J., Cook, N. G. W., and Zimmerman, R. 2007. *Fundamentals of Rock Mechanics*. Fourth edition by Blackwell Publishing. 475.

Jackson, P.B. and Murphey, C.E. 1993. Effect of Casing Pressure on Gas Flow Through a Sheath of Set Cement. Paper SPE 25698 presented at the SPE Drilling Conference, Amsterdam, 23–25 February. doi: 10.2118/25698-MS.

Kirsch. 1898. Die Theorie der Elastizitat und die Bedurfnisse der Festigkeitslehre. Zeitschrift des Vereines deutscher Ingenieure 42, 797-807.

Lavrov, A., Todorovic, J., and Torsæter, M. 2015. Numerical Study of Tensile Thermal Stresses in a Casing-Cement-Rock System with Heterogeneities. Presented at the 49th US Rock Mechanics/Geomechanics Symposium, San Francisco, California. June 28 – July 1.

Li, Y., & Nygaard, R. 2017. A numerical study on the feasibility of evaluating CO2 injection wellbore integrity through casing deformation monitoring. *Greenhouse Gases: Science and Technology*, *8*(1), 51-62.

Nelson, E. B. 1990. *Well cementing. Development of petroleum Science* (Vol. 28. Elsevier Science, 600.

Nelson, E. B., & Guillot, D. (2006). *Well Cementing 2nd edition*: Schlumberger 773.

Nygaard, R., Salehi, S., and Lavoie, R.G. 2011. Effect of Dynamic Loading on Wellbore Leakage for the Wabamun Area CO2 Sequestration Project. Presented at the Canadian Unconventional Resources Conference, Calgary, Alberta, Canada. November 15-17. https://doi.org/10.2118/146640-MS.

Nygaard, R., Salehi, S., Weideman, B. et al. 2014. Effect of Dynamic Loading on Wellbore Leakage for the Wabamun Area CO2-Sequestration Project. *Journal of Canadian Petroleum Technology* 53 (01): 69-82. https://doi.org/10.2118/146640-PA.

Pattillo, P.D. and Kristiansen, T.G. 2002. Analysis of Horizontal Casing Integrity in the Valhall Field. Paper SPE 78204 presented at the SPE/ISRM Rock Mechanics Conference, Irving, Texas, USA, 20–23 October. doi: 10.2118/78204-MS.

Ravi, K., Bosma, M., and Gastebled, O. 2002. Improve the Economics of Oil and Gas Wells by Reducing the Risk of Cement Failure. Paper SPE 74497 presented at the IADC/SPE Drilling Conference, Dallas, 26–28 February. doi: 10.2118/74497-MS.

Saint-Marc, J., Garnier, A., and Bois, A.-P. 2008. Initial State Of Stress: The Key to Achieving Long-Term Cement-Sheath Integrity. Paper SPE 116651 presented at the SPE Annual Technical Conference and Exhibition, Denver, 21–24 September. doi: 10.2118/116651-MS.

Salehi, S., & Nygaard, R. (2015). Full fluid–solid cohesive finite-element model to simulate near wellbore fractures. *Journal of Energy Resources Technology*, *137*(1), 012903. doi:10.1115/1.4028251.

Smith, D. K. 1987. *Cementing*: H.L. Doherty Memorial Fund of AIME, Society of Petroleum Engineers. 254.

Smith, R. C. 1984. Successful Primary Cementing Can Be a Reality. *Journal of Petroleum Technology* 36 (11): 1851-1858. https://doi.org/10.2118/13498-PA.

Terzaghi, K. V. 1936. Stress distribution in dry and saturated sand above a yielding trap door. In: Proc. Int. Conference on Soil Mechanics and Foundation Engineering, Cambridge, MA, vol 1, pp. 307-311.

Terzaghi, K. (1951). *Theoretical soil mechanics*. Chapman And Hall, Limited.; London. 528.

Thiercelin, M.J., Dargaud, B., Baret, J.F., and Rodriquez, W.J. 1998. Cement Design Based on Cement Mechanical Response. SPE Drill & Compl 13 (4): 266–273. SPE-52890-PA. doi: 10.2118/ 52890-PA.

Watson, T. L. and Bachu, S. 2009. Evaluation of the Potential for Gas and CO2 Leakage Along Wellbores. *SPE Drilling & Completion* 24 (01): 115-126. https://doi.org/10.2118/106817-PA.

Weideman, B., & Nygaard, R. 2014. How cement operations affect your cement sheath short and long term integrity. Paper presented at the American Association of Drilling Engineers Fluids Technical Conference and Exhibition. April 15-16.

Weideman, B. L. 2014. Investigation of cased wellbore integrity in the Wabamun area sequestration project. (unpublished master's thesis). Missouri University of Science and Technology, Rolla, Missouri. http://scholarsmine.mst.edu/masters_theses/7284/.

Zhang, H., Sun, B., Yan, G., Wang, Z., & Huang, M. 2016. Distribution laws and effects analysis of casing external pressure taking elastic parameters matching into account. *Petroleum*, *2*(1), 108-115.

Zhang, W., Eckert, A., and Liu, X. 2017. Numerical Simulation of Micro-Annuli Generation by Thermal Cycling. Presented at the 51st US Rock Mechanics/Geomechanics Symposium, San Francisco, California. June 25-28.

APPENDICES

APPENDIX A

Table A.1: Raw data from Chapter 5.4.

	Shallow						Medium			Deep		
All values are in MPa	Radial Casing/ Cement	Hoop Casing/ Cement	Radial Cement/ Rock	Hoop Cement/ Rock	Radial Casing/ Cement	Hoop Casing/ Cement	Radial Cement/ Rock	Hoop Cement/ Rock	Radial Casing/ Cement	Hoop Casing/ Cement	Radial Cement/ Rock	Hoop Cement/ Rock
Base case	0.583	0.897	0.618	0.825	-2.747	5.696	-0.836	3.704	-1.135	15.218	2.442	12.673
Cement Stress	0.470	0.087	0.371	0.151	-3.414	2.210	-2.156	0.875	-2.948	3.495	-1.173	2.684
	0.498	0.288	0.432	0.318	-3.247	3.085	-1.825	1.586	-2.494	6.429	-0.268	5.184
	0.526	0.488	0.493	0.485	-3.081	3.953	-1.496	2.290	-2.042	9.356	0.634	7.678
	0.555	0.696	0.557	0.658	-2.913	4.828	-1.165	3.000	-1.588	12.291	1.539	10.178
	0.583	0.897	0.618	0.825	-2.747	5.696	-0.836	3.704	-1.135	15.218	2.442	12.673
	0.595	0.981	0.644	0.896	-2.314	7.964	0.023	5.545	-0.451	19.642	3.808	16.442
	0.606	1.066	0.670	0.966	-1.880	10.231	0.882	7.385	0.235	24.073	5.176	20.217
	0.618	1.151	0.696	1.037	-1.446	12.499	1.742	9.226	0.919	28.497	6.542	23.986
	0.630	1.236	0.721	1.107	-1.013	14.767	2.601	11.066	1.604	32.921	7.909	27.755
Pore Pressure Rock	0.583	0.897	0.618	0.825	-2.747	5.696	-0.836	3.704	-1.135	15.218	2.442	12.673
	0.583	0.897	0.618	0.825	-2.747	5.696	-0.836	3.704	-1.135	15.218	2.442	12.673
	0.583	0.897	0.618	0.825	-2.747	5.696	-0.836	3.704	-1.135	15.218	2.442	12.673
	0.583	0.897	0.618	0.825	-2.747	5.696	-0.836	3.704	-1.135	15.218	2.442	12.673
	0.583	0.897	0.618	0.825	-2.747	5.696	-0.836	3.704	-1.135	15.218	2.442	12.673
	0.583	0.897	0.618	0.825	-2.747	5.696	-0.836	3.704	-1.135	15.218	2.442	12.673
	0.583	0.897	0.618	0.825	-2.747	5.696	-0.836	3.704	-1.135	15.218	2.442	12.673
	0.583	0.897	0.618	0.825	-2.747	5.696	-0.836	3.704	-1.135	15.218	2.442	12.673
	0.583	0.897	0.618	0.825	-2.747	5.696	-0.836	3.704	-1.135	15.218	2.442	12.673
E Cement	0.577	0.904	0.619	0.832	-2.241	4.926	-0.618	3.233	-0.107	14.270	3.053	12.030
	0.579	0.903	0.619	0.830	-2.393	5.118	-0.693	3.344	-0.433	14.494	2.842	12.169
	0.580	0.901	0.619	0.828	-2.526	5.310	-0.752	3.460	-0.705	14.728	2.678	12.325
	0.582	0.899	0.618	0.827	-2.643	5.503	-0.799	3.581	-0.936	14.971	2.547	12.494
	0.583	0.897	0.618	0.825	-2.747	5.696	-0.836	3.704	-1.135	15.218	2.442	12.673
	0.584	0.895	0.617	0.824	-2.842	5.887	-0.866	3.829	-1.310	15.468	2.358	12.857
	0.583	0.897	0.618	0.825	-2.747	5.696	-0.836	3.704	-1.479	15.708	2.277	13.034
	0.586	0.891	0.616	0.820	-3.036	6.243	-0.936	4.056	-1.135	15.218	2.442	12.673
	0.586	0.889	0.616	0.819	-3.128	6.412	-0.970	4.163	-1.796	16.164	2.130	13.379
PR Cement	0.587	0.974	0.637	0.888	-2.780	6.667	-0.631	4.443	-1.103	17.649	2.871	14.652
	0.586	0.953	0.633	0.871	-2.761	6.400	-0.679	4.243	-1.094	16.987	2.770	14.116
	0.586	0.938	0.629	0.859	-2.747	5.696	-0.836	3.704	-1.096	16.516	2.690	13.734
	0.584	0.914	0.623	0.840	-2.747	5.696	-0.836	3.704	-1.113	15.760	2.550	13.117

	0.583	0.897	0.618	0.825	-2.747	5.696	-0.836	3.704	-1.135	15.218	2.442	12.673
	0.583	0.897	0.618	0.825	-2.747	5.696	-0.836	3.704	-1.186	14.337	2.254	11.949
	0.583	0.897	0.618	0.825	-2.771	5.095	-0.996	3.237	-1.233	13.698	2.109	11.421
	0.574	0.812	0.593	0.755	-2.803	4.680	-1.119	2.910	-1.327	12.648	1.857	10.552
	0.571	0.786	0.585	0.733	-2.747	5.696	-0.836	3.704	-1.408	11.876	1.661	9.910
	0.583	0.897	0.618	0.825	-2.747	5.696	-0.836	3.704	-0.509	15.722	3.152	13.260
	0.578	0.892	0.611	0.820	-2.394	5.978	-0.510	4.000	-0.678	15.586	2.956	13.096
	0.580	0.894	0.614	0.822	-2.508	5.886	-0.614	3.905	-0.828	15.465	2.782	12.952
	0.581	0.895	0.616	0.824	-2.747	5.696	-0.836	3.704	-0.975	15.346	2.614	12.814
E Rock	0.583	0.897	0.618	0.825	-2.747	5.696	-0.836	3.704	-1.135	15.218	2.442	12.673
	0.584	0.898	0.620	0.827	-2.747	5.696	-0.836	3.704	-1.278	15.102	2.288	12.546
	0.585	0.899	0.621	0.828	-2.955	5.530	-1.030	3.529	-1.408	14.998	2.149	12.432
	0.586	0.900	0.623	0.829	-3.045	5.459	-1.114	3.454	-1.526	14.903	2.023	12.329
	0.586	0.901	0.624	0.830	-2.747	5.696	-0.836	3.704	-1.633	14.817	1.908	12.235
	0.583	0.897	0.618	0.826	-2.834	5.627	-0.919	3.632	-1.238	15.135	2.342	12.579
	0.583	0.897	0.618	0.826	-2.808	5.647	-0.895	3.653	-1.206	15.160	2.373	12.608
	0.583	0.897	0.618	0.825	-2.784	5.667	-0.871	3.674	-1.135	15.218	2.442	12.673
	0.583	0.897	0.618	0.825	-2.769	5.679	-0.857	3.686	-1.159	15.198	2.419	12.650
PR Rock	0.583	0.897	0.618	0.825	-2.747	5.696	-0.836	3.704	-1.135	15.218	2.442	12.673
	0.583	0.897	0.618	0.825	-2.728	5.711	-0.818	3.720	-1.115	15.234	2.461	12.691
	0.583	0.897	0.618	0.825	-2.717	5.720	-0.807	3.729	-1.105	15.242	2.470	12.701
	0.583	0.897	0.618	0.825	-2.705	5.730	-0.794	3.739	-1.097	15.248	2.477	12.710
	0.583	0.897	0.619	0.825	-2.699	5.734	-0.788	3.744	-1.101	15.245	2.472	12.708
	0.583	0.897	0.618	0.825	-2.746	5.696	-0.832	3.703	-1.132	15.219	2.455	12.665
	0.583	0.897	0.618	0.825	-2.747	5.696	-0.836	3.704	-1.134	15.218	2.452	12.666
	0.583	0.897	0.618	0.825	-2.748	5.695	-0.834	3.703	-1.136	15.217	2.449	12.666
	0.583	0.897	0.618	0.825	-2.748	5.695	-0.835	3.703	-1.138	15.215	2.445	12.667
Isotropic Variation	0.583	0.897	0.618	0.825	-2.747	5.696	-0.836	3.704	-1.140	15.214	2.442	12.667
	0.583	0.897	0.618	0.825	-2.749	5.694	-0.837	3.703	-1.142	15.213	2.439	12.668
	0.583	0.897	0.618	0.825	-2.750	5.694	-0.838	3.703	-1.144	15.212	2.436	12.668
	0.583	0.897	0.618	0.825	-2.750	5.694	-0.839	3.703	-1.146	15.210	2.432	12.669
	0.583	0.897	0.618	0.825	-2.751	5.694	-0.840	3.703	-1.148	15.209	2.429	12.669
	0.583	0.897	0.618	0.825	-2.747	5.696	-0.836	3.704	-1.125	15.224	2.456	12.673
	0.583	0.897	0.618	0.825	-2.747	5.696	-0.836	3.704	-1.127	15.223	2.453	12.674
	0.583	0.897	0.618	0.825	-2.746	5.697	-0.834	3.705	-1.128	15.222	2.449	12.675
	0.583	0.897	0.618	0.825	-2.746	5.697	-0.835	3.705	-1.130	15.221	2.446	12.676
Anisotropic Variation	0.583	0.897	0.618	0.825	-2.746	5.697	-0.836	3.705	-1.132	15.220	2.443	12.677
	0.583	0.897	0.618	0.825	-2.747	5.697	-0.837	3.705	-1.135	15.218	2.442	12.673
	0.583	0.897	0.618	0.825	-2.747	5.696	-0.836	3.704	-1.135	15.218	2.436	12.678
	0.583	0.897	0.618	0.825	-2.748	5.696	-0.839	3.706	-1.135	15.218	2.442	12.673
	0.583	0.897	0.618	0.825	-2.748	5.696	-0.840	3.706	-1.135	15.218	2.442	12.673
	0.583	0.897	0.618	0.825	-2.746	5.696	-0.831	3.703	-1.130	15.220	2.458	12.665
	0.583	0.897	0.618	0.825	-2.746	5.696	-0.832	3.703	-1.131	15.220	2.457	12.665
	0.583	0.897	0.618	0.825	-2.747	5.696	-0.836	3.704	-1.131	15.220	2.457	12.665
	0.583	0.897	0.618	0.825	-2.746	5.696	-0.832	3.703	-1.132	15.219	2.456	12.665
Vertical Variation	0.583	0.897	0.618	0.825	-2.746	5.696	-0.832	3.703	-1.132	15.219	2.455	12.665
	0.583	0.897	0.618	0.825	-2.747	5.696	-0.833	3.703	-1.135	15.218	2.442	12.673
	0.583	0.897	0.618	0.825	-2.747	5.696	-0.833	3.703	-1.133	15.218	2.454	12.666
	0.583	0.897	0.618	0.825	-2.747	5.696	-0.833	3.703	-1.134	15.218	2.453	12.666
	0.583	0.897	0.618	0.825	-2.747	5.696	-0.833	3.703	-1.134	15.218	2.452	12.666
	-0.464	1.271	-0.151	0.927	-5.865	7.158	-2.885	4.104	-6.359	17.165	-1.563	13.326

Internal Casing Pressure	-0.201	1.177	0.042	0.901	-5.086	6.792	-2.373	4.004	-1.135	15.218	2.442	12.673
	0.062	1.083	0.235	0.876	-4.306	6.427	-1.861	3.904	-3.749	16.192	0.438	13.000
	0.325	0.989	0.428	0.850	-3.527	6.061	-1.348	3.804	-2.444	15.706	1.439	12.836
	0.583	0.897	0.618	0.825	-2.747	5.696	-0.836	3.704	-1.135	15.218	2.442	12.673
	0.846	0.803	0.811	0.800	-1.968	5.330	-0.323	3.604	0.171	14.731	3.444	12.509
	1.109	0.708	1.004	0.774	-1.188	4.964	0.189	3.504	1.477	14.244	4.446	12.346
	1.371	0.614	1.197	0.749	-0.408	4.599	0.702	3.404	2.787	13.756	5.450	12.182
	1.634	0.520	1.390	0.723	0.373	4.233	1.216	3.304	4.094	13.269	6.454	12.018
Pore Pressure Cement	5.153	5.467	5.188	5.395	33.103	41.546	35.014	39.554	48.735	65.088	52.312	62.543
	4.013	4.327	4.048	4.255	24.143	32.586	26.054	30.594	36.265	52.618	39.842	50.073
	2.863	3.177	2.898	3.105	15.173	23.616	17.084	21.624	23.795	40.148	27.372	37.603
	1.723	2.037	1.758	1.965	6.213	14.656	8.124	12.664	11.335	27.688	14.912	25.143
	0.583	0.897	0.618	0.825	-2.747	5.696	-0.836	3.704	-1.135	15.218	2.442	12.673
	0.323	0.637	0.358	0.565	-3.897	4.546	-1.986	2.554	-5.075	11.278	-1.498	8.733
	0.063	0.377	0.098	0.305	-5.037	3.406	-3.126	1.414	-9.005	7.348	-5.428	4.803
	-0.207	0.107	-0.172	0.035	-6.187	2.256	-4.276	0.264	-12.945	3.408	-9.368	0.863
	-0.467	-0.153	-0.432	-0.225	-7.327	1.116	-5.416	-0.876	-16.875	-0.522	-13.298	-3.067

VITA

Jarrett Lee Wise

Candidate for the Degree of

Master of Science

Thesis: WELLBORE INTEGRITY AND CEMENT SHEATH DEBONDING ANALYSIS FOR WELLS IN THE EUGENE ISLAND OPD, GULF OF MEXICO

Major Field: Petroleum Engineering

Biographical:

Education:

Completed the requirements for the Master of Science in Petroleum Engineering at Oklahoma State University, Stillwater, Oklahoma in May, 2019.

Completed the requirements for the Bachelor of Arts in Physics at Hastings College, Hastings, Nebraska in May, 2014.

Experience:

Product Compounder at Platte Valley Energetics, June 2016 – Aug. 2017.

Production Coordinator: UltraFloat Division at Hastings Irrigation Pipe Company, Feb. 2016 – May 2016.

Graduate Research Assistant at University of Wyoming, Sept. 2014 – Aug. 2015.